Petrogenesis of Dacites in a Triassic Volcanic Arc in the South China Sea: Constraints From Whole Rock and Mineral Geochemistry

Wu Wei[1,2], Chuan-Zhou Liu[1,3,2]*, Ross N. Mitchell[1,2] and Wen Yan[4,2]

[1]State Key Laboratory of Lithospheric Evolution, Institute of Geology and Geophysics, Chinese Academy of Sciences, Beijing, China, [2]University of Chinese Academy of Sciences, Beijing, China, [3]CAS Center for Excellence in Deep Earth Science, Guangzhou, China, [4]Key Laboratory of Ocean and Marginal Sea Geology, South China Sea Institute of Oceanology, Chinese Academy of Sciences, Guangzhou, China

Triassic volcanic rocks, including basalts and dacites, were drilled from Meiji Atoll in the South China Sea (SCS), which represents a rifted slice from the active continental margin along the Cathaysia Block. In this study, we present apatite and whole rock geochemistry of Meiji dacites to decipher their petrogenesis. Apatite geochronology yielded U-Pb ages of 204–221 Ma, which are identical to zircon U-Pb ages within uncertainty and thus corroborate the formation of the Meiji volcanic rocks during the Late Triassic. Whole rock major elements suggest that Meiji dacites mainly belong to the high-K calc-alkaline series. They display enriched patterns in light rare earth elements (LREE) and flat patterns in heavy rare earth elements (HREE). They show enrichment in large-ion lithophile elements (LILE) and negative anomalies in Eu, Sr, P, Nb, Ta, and Ti. The dacites have initial $^{87}Sr/^{86}Sr$ ratios of 0.7094–0.7113, $\varepsilon_{Nd}(t)$ values of -5.9–-5.4 and $\varepsilon_{Hf}(t)$ values of -2.9–-1.7, whereas the apatite has relatively higher initial $^{87}Sr/^{86}Sr$ ratios (0.71289–0.71968) and similar $\varepsilon_{Nd}(t)$ (-8.13–-4.56) values. The dacites have homogeneous Pb isotopes, with initial $^{206}Pb/^{204}Pb$ of 18.73–18.87, $^{207}Pb/^{204}Pb$ of 15.75–15.80, and $^{208}Pb/^{204}Pb$ of 38.97–39.17. Modeling results suggest that Meiji dacites can be generated by <40% partial melting of amphibolites containing ~10% garnet. Therefore, we propose that the Meiji dacites were produced by partial melting of the lower continental crust beneath the South China block, triggered by the underplating of mafic magmas as a response to Paleo-Pacific (Panthalassa) subduction during the Triassic. Meiji Atoll, together with other microblocks in the SCS, were rifted from the South China block and drifted southward due to continental extension and the opening of the SCS.

Keywords: dacites, apatite, volcanic arc, Paleo-Pacific subduction, Late Triassic, South China sea

INTRODUCTION

As one of the largest marginal basins, the South China Sea (SCS) in the western Pacific (~3,500,000 km²) has been extensively studied in recent years (e.g., Taylor and Hayes, 1983; Savva et al., 2014; Zhang G.-L. et al., 2018; Ye et al., 2018; Ding et al., 2020; Cui et al., 2021; Miao et al., 2021). It has been suggested that the South China block (SCB) experienced extension and rifting since the Mesozoic, which finally resulted in formation of the SCS (Taylor and Hayes, 1983; Li

Z.-X. et al., 2012; Ding et al., 2018; Fan et al., 2020). Magmatism plays a significant role in plate reconstruction and understanding regional tectonic evolution. Previous work mainly focused on the spreading ridges and the Cenozoic continental margins of the SCS region as the former contain significant hydrocarbon reservoirs (Fan et al., 2020). Research on the pre-Cenozoic igneous activity and structural evolution of the SCS region is relatively limited, particularly for the southern continental margin of the SCS that split off from the Eurasian margin by the opening of the SCS in the Cenozoic. Before the initial rifting and seafloor spreading, the SCS region is considered to be a convergent continental margin with an Andean-type volcanic arc during much of the Jurassic and Cretaceous, and thus then represented the southernmost extent of the South China mainland (Holloway, 1982). In contrast, outside of the SCS area, Permian–Triassic volcanic rocks have rarely been reported along the eastern coastal region of the SCB, which is interpreted to be the result of high rates of tectonic uplift and erosion of the active continental margin volcanic arc (Yamamoto et al., 2009; Safonova et al., 2015; Gao W. et al., 2017). However, the northern and southern continental margins of the SCS that opened during the Cenozoic preserve the record of late Mesozoic arc magmatism in the SCB related to Paleo-Pacific subduction according to large positive magnetic anomalies and Mesozoic silicic to intermediate arc-related intrusives and volcanic rocks (e.g., Zhou et al., 2006; Yan et al., 2010; Wu et al., 2011; Yan et al., 2014; Xu et al., 2017; Li et al., 2018).

Recently, Mesozoic strata in the northeastern SCS with large thickness, relatively high P-wave velocities, and high densities have been interpreted as the Mesozoic forearc basin based on ocean bottom seismometer (OBS) data, multi-channel seismic data, gravity data, drill hole data, and petrologic observations. The sequence thus constitutes an arc-forearc-accretionary wedge within the SCS region (Fan et al., 2020). It is generally accepted that the southern continental margin of the SCS was once located on the edge of the SCB before the formation of the SCS, sharing a similar tectonic setting to the SCB during the Mesozoic time (Taylor and Hayes, 1983; Briais et al., 1993; Hall, 2002; Ding et al., 2013; Franke et al., 2014; Miao et al., 2021; Wei et al., 2021). Therefore, we speculate that the arc magmatism associated with the active continental margin in the early Mesozoic may be preserved in the SCS region.

In this study, we present the geochemical compositions of Late Triassic dacites drilled on Meiji Atoll in the SCS, including whole rock elemental and isotopic data, and Sr-Nd isotopes of apatite. These data are utilized to decipher the petrogenesis of the dacites and the evolution of the active continental margin of the SCB.

GEOLOGICAL SETTING AND SAMPLE DESCRIPTION

Geological Setting

The South China Sea (SCS) is encircled by three plates (**Figure 1**), i.e., the Philippine Sea plate, the Eurasian plate, and the Indo-Australian plate. It consists of three geological units, i.e., the northern continental margin, the ocean basin, and the southern

continental margin (Yan et al., 2010). It has been suggested that the SCS experienced almost a complete Wilson cycle since the Late Mesozoic, i.e., from continental rifting, through seafloor spreading, and then eastward subduction of the SCS lithosphere under the Philippine Sea plate (Ding et al., 2018). The Cathaysian block had experienced lithospheric extension since the Late Cretaceous (Schlüter et al., 1996; Zhou et al., 2015), and seems to exploited the pre-existing Andean-type arc along the eastern coastal region of the SCB (Clift and Lin, 2001). Deep tow magnetic data and the IODP Expedition 349 drilling results have constrained that seafloor spreading in the SCS was initiated at ca. 33 Ma and terminated by ca. 15 Ma (Li et al., 2014; Ding et al., 2018). The mechanism leading to the opening of the SCS remains highly controversial and different models have been proposed, including tectonic rotation and extrusion of the Indochina Peninsula (Tapponnier et al., 1986; Briais et al., 1993), slab pull of the proto-SCS (Sibuet et al., 2016), back-arc extension (Sun et al., 2018), and the Hainan plume (Xu et al., 2012).

Opening of the SCS also resulted in the south-by-southeastward movements of several micro-blocks, including the Reed Bank-Northeastern Palawan block (Bing-Quan et al., 2004; Barckhausen et al., 2014; Wei et al., 2015). Several micro-blocks constitute the continental margin of the SCS (Yao et al., 2004), including the Zhongsha block (Macclesfield Bank), the Xisha block (Paracel Islands), the Dongsha block (Pratas Reef), the Nansha block (Spratly Islands), and the Reed Bank-Northeastern Palawan block (Yan et al., 2010). Previous studies have inferred the existence of a continental basement underneath the Nansha block and probably all other microblocks in the SCS, based on the Nd model ages of dredged 159–127 Ma granitic rocks and samples from several wells within this area (Yan et al., 2010).

Meiji (i.e., Mischief) Atoll, as a part of the Reed Bank-Northeastern Palawan block, is located on the northeastern margin of the Spratly Islands. Reed Bank is surrounded by thick Cenozoic sedimentary basins extending over an area of about 55,000 km^2. Numerous scattered coral reefs, seamounts, sea knolls, trough valleys, and fault-depressed mesas are distributed throughout the basin floor of Reed Bank, resulting in highly variable topography (Tang et al., 2014). The shear wave velocity structure of a wide-angle seismic profile across Reed Bank along the southern continental margin of the SCS demonstrates a decrease of the Moho depth from 20 to 22 km at Reed Bank to 9–11 km in the deep oceanic basin, indicating marked regional extension in this area (Wei et al., 2015). Numerous petrological, sedimentological, and geophysical lines of evidence all suggested that the southern continental margin of the SCS shares an affinity with the South China mainland before the opening of the SCS basin (Taylor and Hayes, 1980; Holloway, 1982; Kudrass et al., 1986; Hutchison, 2004; Yan et al., 2011; Miao et al., 2021).

Sample Description

The studied dacites were selected from the Nanke-1 core drilled on Meiji Atoll, which penetrated the volcanic basement from 997.70 to 2,020.20 mbsf (meters below seafloor). The recovered volcanic rocks mainly consist of dacites, and minor basalts interbedded with the dacites. Samples in this study were
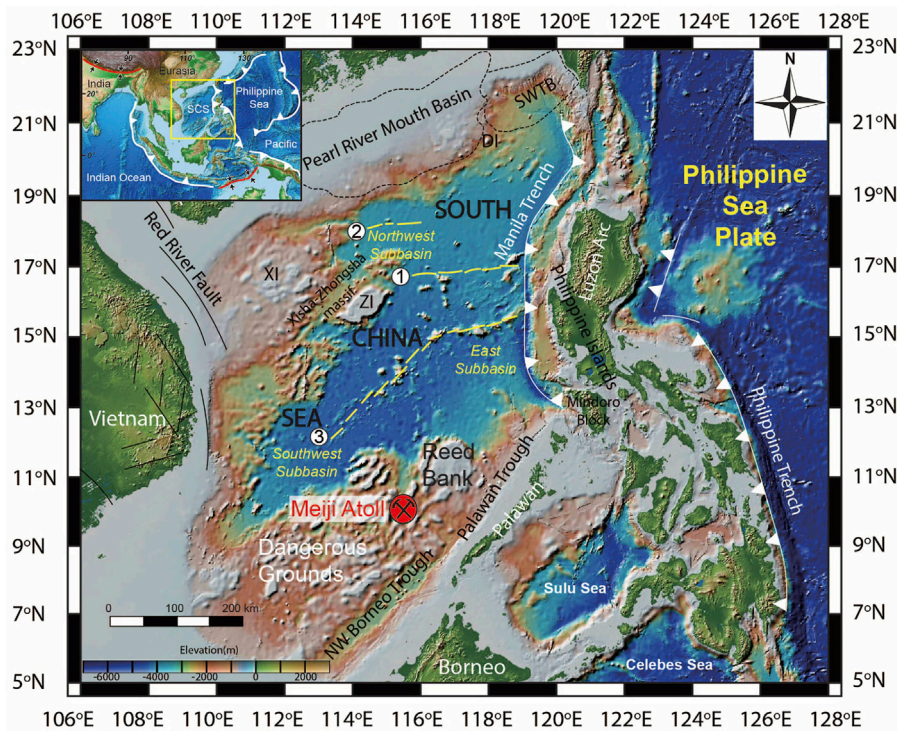
FIGURE 1 | Tectonic sketch map of the area around the South China Sea (after Yu et al., 2018). BBWB, Beibuwan basin; SWTB, Southwest Taiwan basin; XI, Xisha Islands (Paracel Islands); ZI, Zhongsha Islands (Macclesfield Bank); DI, Dongsha Islands (Pratas Islands). White circles 1, 2, and 3 represent the fossil mid-ocean ridge at ages of ca. 33–23.6 Ma, ca. 30–28.5 Ma, and ca. 23.6–15 Ma, respectively. The black solid line represents the lithospheric faults. The white solid line with white triangles represents the subduction zone.

collected from 1,197.20 to 1,502.05 mbsf of the core (**Figure 2**). The dacite samples are phyric in texture and contain abundant coarse-to-medium-grain plagioclase phenocrysts (~10–15 vol%), K-feldspar (2–5%), and quartz (2–5%). Both plagioclase and K-feldspar phenocrysts are subhedral to euhedral in shape, have grain sizes of 0.5–2 mm, exhibit porphyritic to glomerocrystic textures, and have undergone moderate alteration (**Figures 2C,D**). The groundmass is mainly composed of tiny fine-grained plagioclase, quartz, biotite and titanite (**Figure 3C**), with minor secondary minerals of chlorite, sericite, and epidote. The plagioclase shows characteristic polysynthetic twinning under optical microscopy. Opaques, zircon, and apatite are present as accessory minerals.

Apatite ubiquitously occurs as the dominant phosphate accessory mineral in the studied samples, mainly as inclusions within plagioclase and seldom in the groundmass (**Figure 3**). The apatite inclusions are subhedral to euhedral in shape, 25–320 μm in size, whereas the groundmass apatite is 50–200 μm in size. Microtextural features suggest that apatite was an early crystallizing phase.
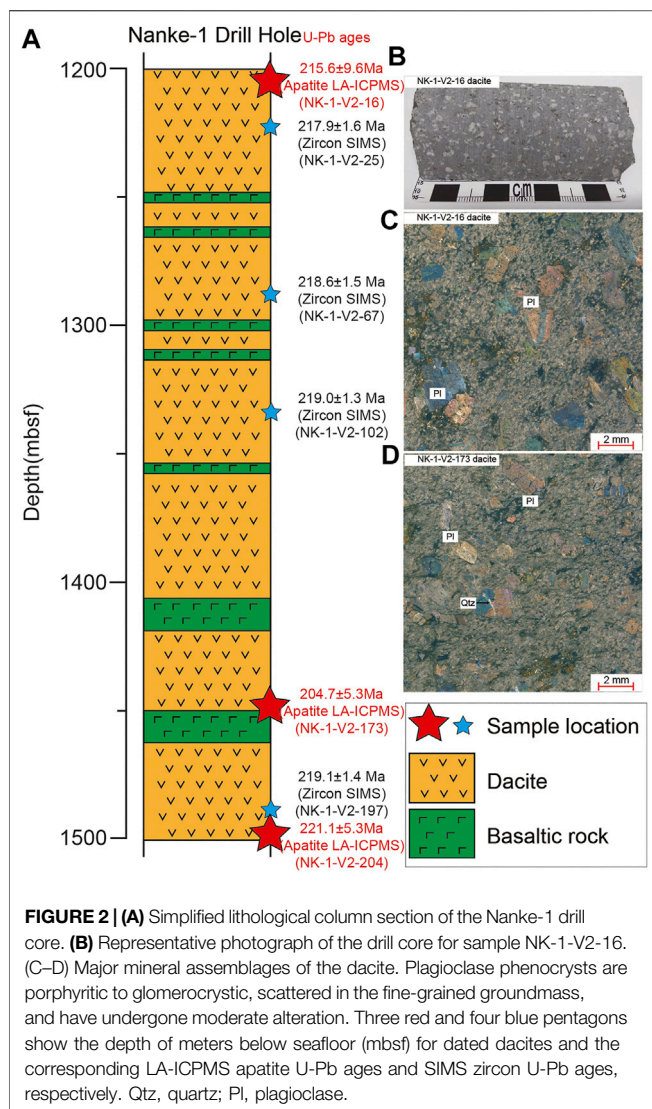
ANALYTICAL METHODS

All measurements were conducted at the Institute of Geology and Geophysics, Chinese Academy of Sciences (IGGCAS).

Apatite Major Elements

Major element compositions of apatite were measured by JEOL-JXA8100 electron microprobe operated with wavelength-dispersive spectrometers (WDS). The operating conditions were 15 kV accelerating voltage, 10 nA beam current, and 10 μm defocused electron beam. Twenty seconds (s) of counting time was used for most elements, except F and Cl that were examined for 10 s in order to avoid volatile loss at their characteristic X-rays. Natural minerals and synthetic oxides were chosen as calibration standards, and all data were corrected based on the ZAF procedure. Analytical accuracy for most elements was better than 1%, whereas for Cl and F it was ~5%.

Apatite U-Pb Dating and Trace Elements

Apatite grains were separated from three dacite samples using conventional hydro-separation and magnetic methods, followed by handpicking under a binocular microscope. The apatite grains were mounted in an epoxy resin disc and afterwards polished to expose their internal sections. These grains were examined and imaged before analysis using an optical microscope under both transmitted and reflected light. Back-scattered electron (BSE) images were acquired to determine internal structure and target positions for *in situ* spot analyses. Apatite U-Pb dating was undertaken by an Agilent 7500a quadruple inductively coupled plasma mass spectrometer (Q-ICP-MS), coupled with a 193 nm excimer ArF laser-ablation system (Geolas HD, Lambda Physik, Göttingen,

FIGURE 2 | (A) Simplified lithological column section of the Nanke-1 drill core. **(B)** Representative photograph of the drill core for sample NK-1-V2-16. **(C–D)** Major mineral assemblages of the dacite. Plagioclase phenocrysts are porphyritic to glomerocrystic, scattered in the fine-grained groundmass, and have undergone moderate alteration. Three red and four blue pentagons show the depth of meters below seafloor (mbsf) for dated dacites and the corresponding LA-ICPMS apatite U-Pb ages and SIMS zircon U-Pb ages, respectively. Qtz, quartz; Pl, plagioclase.

Germany). The detailed procedure has been previously described (Yang et al., 2009). A spot diameter of 60 μm, a repetition rate of 6 Hz, and a fluence of 6.5 J/cm² were used. Two apatite standards, NW-1 (1,160 ± 5 Ma; Li Q.-L. et al., 2012) and McClure Mountain (523.51 ± 1.47 Ma; Chew et al., 2014), were analyzed to correct downhole U–Pb fractionation, mass bias, and intra-session instrument drift. For trace element analyses, ^{43}Ca was used as an internal standard and NIST SRM 610 reference glass was used as an external standard. The CaO content in apatites was determined by electron microprobe analysis. The GLITTER program (GEMOC, Macquarie University; Griffin et al., 2008) was used for age and trace element data reduction. Tera-Wasserburg plots and age calculations were generated using Isoplot 3.0 (Ludwig, 2000).
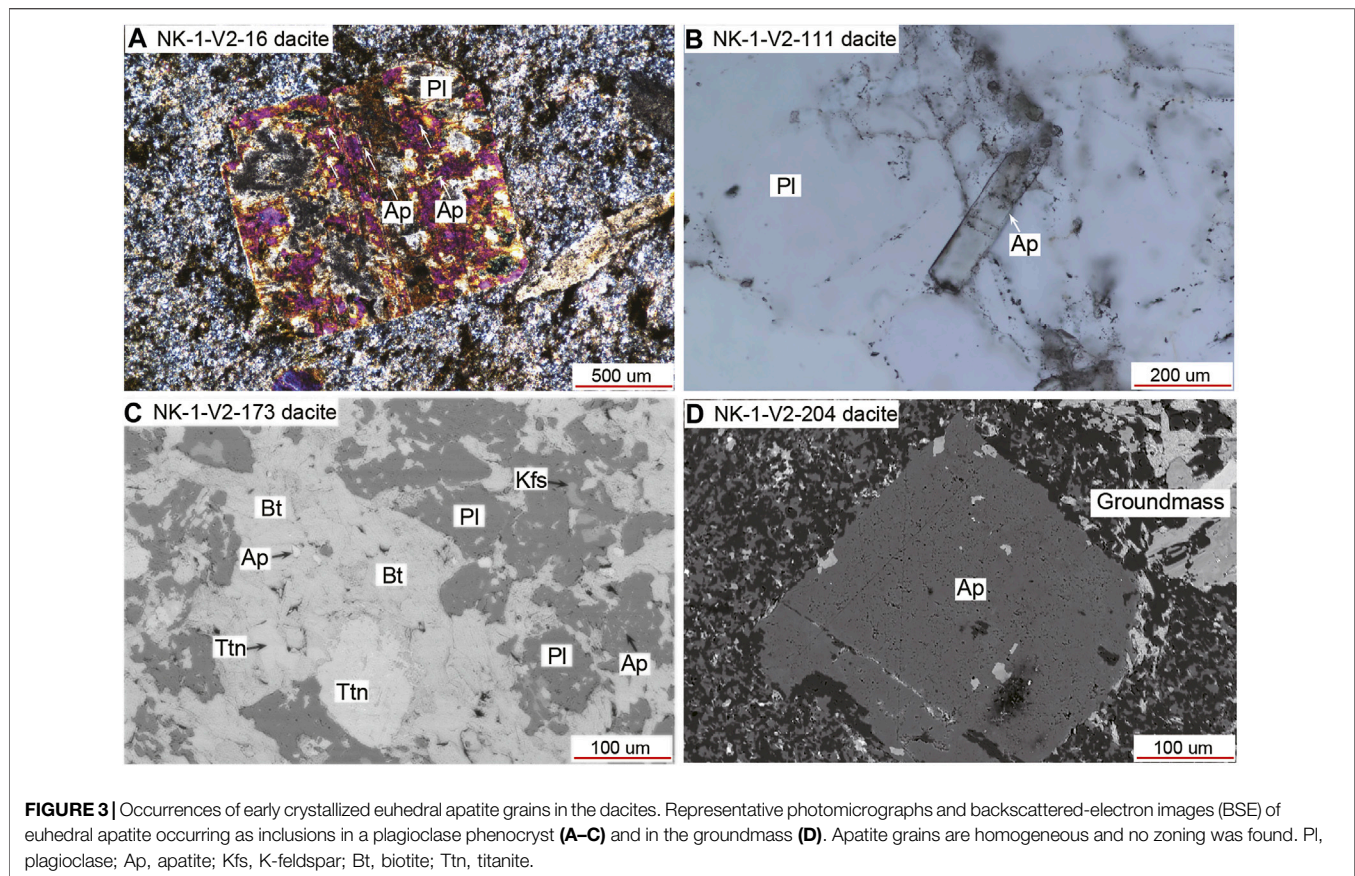
Apatite Sr-Nd Isotopes

In-situ analyses of Sr and Nd isotopes in apatite were conducted using a Thermo Scientific Neptune multi-collector inductively coupled plasma mass spectrometer (MC-ICP-MS), coupled with a 193 nm ArF Excimer laser-ablation system (Geolas HD,

Lambda Physik, Göttingen, Germany). A spot size of 60 μm and a pulse rate of 6 Hz were used. The detailed procedure has been previously described (Yang et al., 2008). A typical data acquisition cycle consisted of a 30 s measurement of the Kr gas blank with the laser switched off, followed by 60 s of measurement with the laser ablating. Data reduction was conducted offline and the potential isobaric interferences were accounted for in the following order: Kr, Yb^{2+}, Er^{2+} and Rb. Finally, the $^{87}Sr/^{86}Sr$ ratios were calculated and normalized from the interference-corrected $^{86}Sr/^{88}Sr$ ratio using an exponential law. The whole data reduction procedure was performed using an in house Excel VBA (Visual Basic for Applications) macro program. Two apatite reference materials, Slyudyanka and AP1, were measured along with the samples and yielded $^{87}Sr/^{86}Sr$ ratios of 0.70761 ± 19 (2SD, $n = 20$) and 0.711,315 ± 20 (2SD, $n = 18$), respectively, which are consistent with their respective reference values of 0.70769 ± 15 and 0.711,370 ± 31 (Yang et al., 2014).

In order to obtain accurate $^{147}Sm/^{144}Nd$ and $^{143}Nd/^{144}Nd$ data by LA-MC-ICP-MS, care must be taken to adequately correct for the contribution of the isobaric interference of ^{144}Sm on the ^{144}Nd signal. The Sm interference correction is complicated by the fact that the $^{146}Nd/^{144}Nd$ ratio, which is conventionally used to normalize the other Nd isotope ratios, is also affected by Sm interference. As a result, the mass bias correction of ^{144}Sm interference on ^{144}Nd cannot be applied directly from the measured $^{146}Nd/^{144}Nd$ ratio. In this work, we have adopted the recently revised Sm isotopic abundances ($^{147}Sm/^{149}Sm =$ 1.08680 and $^{144}Sm/^{149}Sm = 0.22332$) (Yang et al., 2014). Firstly, we used the measured $^{147}Sm/^{149}Sm$ ratio to calculate the Sm fractionation factor and the measured ^{147}Sm intensity by employing the natural $^{147}Sm/^{144}Sm$ ratio of 4.866,559 to estimate the Sm interference on mass 144. Then the interference-corrected $^{146}Nd/^{144}Nd$ ratio can be used to calculate the Nd fractionation factor. Finally, the $^{143}Nd/^{144}Nd$ and $^{145}Nd/^{144}Nd$ ratios were normalized using the exponential law. The $^{147}Sm/^{144}Nd$ ratio of unknown samples can also be calculated using the exponential law after correcting for isobaric interference of ^{144}Sm on ^{144}Nd as described above. The raw data were exported offline and the whole data reduction procedure was performed using an in house Excel VBA (Visual Basic for Applications) macro program. Two apatite reference materials, Otter Lake and Mud Tank, were measured along with the samples and yielded $^{143}Nd/^{144}Nd$ ratios of 0.511,925 ± 51 (2SD, $n = 15$) and 0.512,324 ± 130 (2SD, $n = 10$), respectively, which are consistent with their respective reference values of 0.511,942 ± 45 and 0.512,361 ± 111 (Yang et al., 2014).

Whole-Rock Major and Trace Elements

The dacite samples were crushed and then powdered to a grain size of 200 mesh in an agate mill for whole rock analyses. Bulk-rock major element compositions were determined on fused lithium–tetraborate glass beads, using the AXIOS Minerals X-ray fluorescence (XRF) spectrometer. The analytical precision for the concentrations of major elements ranges from 1 to 3%. Concentrations of whole rock trace elements were analyzed by an Agilent 7500a inductively coupled plasma

FIGURE 3 | Occurrences of early crystallized euhedral apatite grains in the dacites. Representative photomicrographs and backscattered-electron images (BSE) of euhedral apatite occurring as inclusions in a plagioclase phenocryst **(A–C)** and in the groundmass **(D)**. Apatite grains are homogeneous and no zoning was found. Pl, plagioclase; Ap, apatite; Kfs, K-feldspar; Bt, biotite; Ttn, titanite.

mass spectrometer (ICP-MS), following the procedure of Yang et al. (2012). The powdered samples (about 50 mg) were dissolved in high-pressure Teflon vessels using a highly purified HF + HNO_3 mixture for 5 days at 150 C. Rh was added as an internal standard to monitor signal drift during analysis. Standard materials BIR-1a, RGM-2, GSR-3, and BHVO-2 were analyzed as unknown samples to monitor the accuracy of data, and indicated the analytical uncertainties were better than 5%.
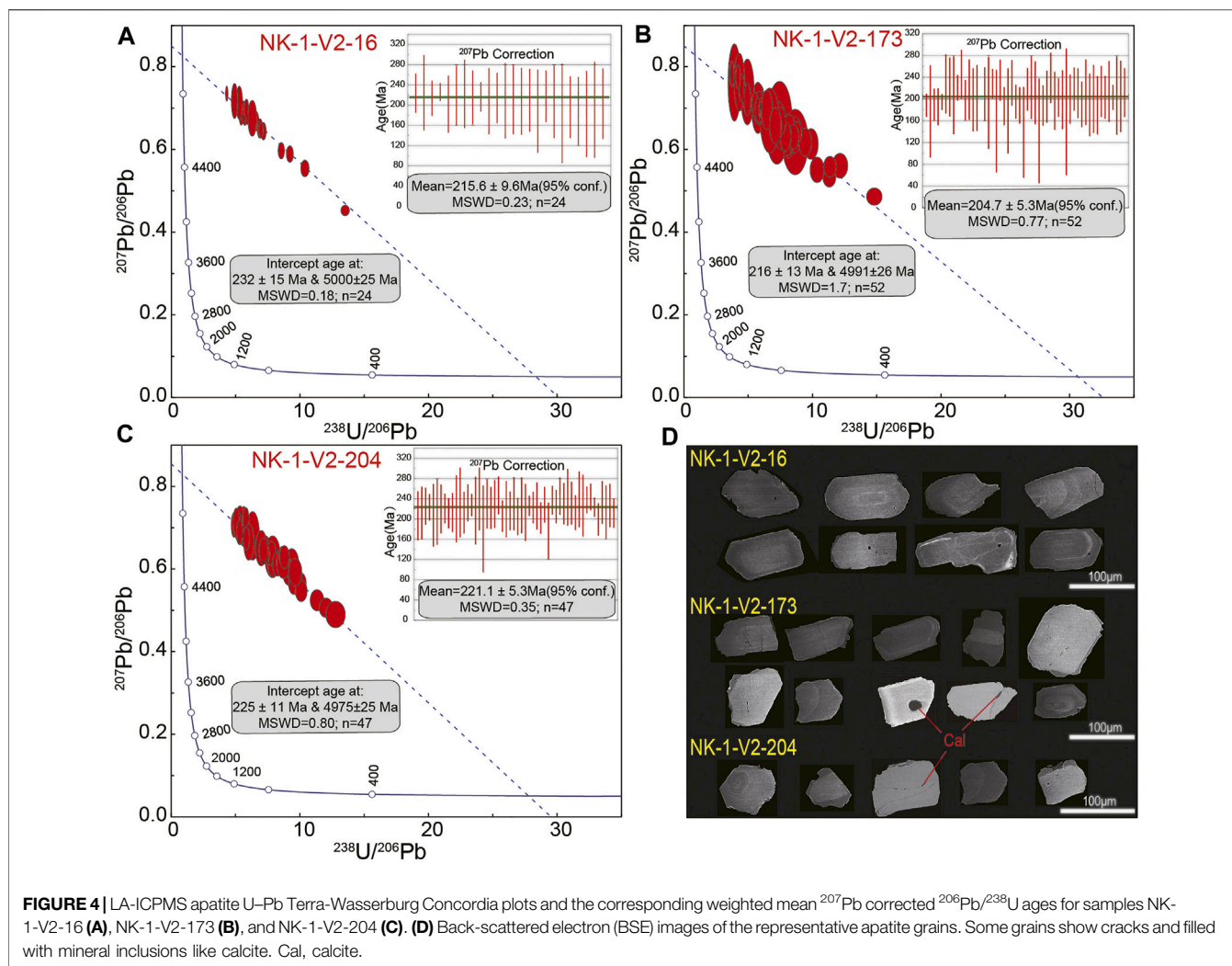
Whole-Rock Sr-Nd-Hf-Pb Isotopes

Sr-Nd-Hf isotopic ratios were measured on a Neptune Plus MC-ICPMS, following the procedure of Yang et al. (2010). About 100 mg sample powders were dissolved in high-pressure Teflon vessels using a highly purified concentrated HF + HNO_3+$HClO_4$ (2 ml + 1 ml + 0.2 ml) mixture for 7 days at 150°C. The solutions then were evaporated to fume $HClO_4$, after which 1 ml 6 M HCl was added and dried, and then this procedure was repeated one time. After cooling down, 5 ml of 3 M HCl was added to the residue, which was put on a hot plate at 100°C for 12 h. Then the sample solutions were loaded onto pre-conditioned 2 ml Ln Spec resins. The light and middle rare earth elements (LMREE) were firstly eluted out, then followed by the Lu (+Yb) fraction. After separating the Ti from Hf using a 4M HCl+0.5% H_2O_2 mixture, Hf (+Zr) was extracted from the column with HF. After drying the Hf (+Zr) solution, 1 ml of 2% HNO_3 was added to the residue for Hf analysis. The solution of LMREE was dried and re-dissolved in 1.5 ml of 2.5 M HCl. After

loading the solution into a quartz column packed with AG50W-X12, Rb and Sr were eluted with 1.5 ml of 5M HCl and 3 ml of 5M HCl, respectively. Then the LMREE fraction was stripped out with 6 ml of 6 M HCl. After the LMREE collections were dried and re-dissolved in 0.5 ml of 0.25 M HCl, the solutions were loaded onto another commercial Ln Spec resin column (100–150 µm particle size, 2 ml) to elute Nd and Sm with 6 ml of 0.25M HCl and 10 ml of 0.4M HCl, respectively.

The $^{87}Sr/^{86}Sr$, $^{143}Nd/^{144}Nd$ and $^{176}Hf/^{177}Hf$ ratios were normalized to $^{86}Sr/^{88}Sr$ = 0.1194, $^{146}Nd/^{144}Nd$ = 0.7219 and $^{179}Hf/^{177}Hf$ = 0.7325, respectively, using the exponential law. During the analytical sessions, the measured values for NBS987 Sr standard, JNdi-1 Nd standard, and Alfa Hf standard were 0.710,277 ± 24 (2SD, n = 10) for $^{87}Sr/^{86}Sr$, 0.512,107 ± 10 (2SD, n = 10) for $^{143}Nd/^{144}Nd$, and 0.282,192 ± 14 (2SD, n = 12) for $^{176}Hf/^{177}Hf$. In addition, USGS reference materials BHVO-2 and BIR-1 were also processed for Sr–Nd–Hf isotopes, and gave ratios of 0.703,481 ± 12 (2SD, n = 4) and 0.703,101 ± 11 (2SD, n = 4) for $^{87}Sr/^{86}Sr$, 0.512,987 ± 12 (2SD, n = 4) and 0.513,124 ± 13 (2SD, n = 4) for $^{143}Nd/^{144}Nd$ and 0.283,087 ± 10 (2SD, n = 4) and 0.283,247 ± 20 (2SD, n = 4) for $^{176}Hf/^{177}Hf$, respectively, which is identical, within error, to the recommended values (Jochum et al., 2005). The total procedure blanks for Sr, Nd, and Hf were 240 pg, 70 pg, and 50 pg, respectively.

The Pb isotopes were measured on a Thermo-Fisher Triton Plus thermal ionization mass spectrometer (TIMS) following the

FIGURE 4 | LA-ICPMS apatite U–Pb Terra-Wasserburg Concordia plots and the corresponding weighted mean ^{207}Pb corrected ^{206}Pb/^{238}U ages for samples NK-1-V2-16 **(A)**, NK-1-V2-173 **(B)**, and NK-1-V2-204 **(C)**. **(D)** Back-scattered electron (BSE) images of the representative apatite grains. Some grains show cracks and filled with mineral inclusions like calcite. Cal, calcite.

procedure of Li et al. (2015). About 100–120 mg sample powders were dissolved in Savillex Teflon screw-cap beakers using a highly purified concentrated HF + HNO$_3$ mixture for 7 days at 160°C. The Pb fraction was separated from the matrix using the HBr-HCl elution procedure in Teflon columns containing ~0.15 ml anion resin (AG1-X8, 100–200 mesh), which was re-dissolved using a mixture solution of silica gel and H$_3$PO$_4$.

The whole chemical procedural blank for Pb was approximately 200 pg. The standard NIST 981 was used to monitor instrument stability during data collection and to correct mass fractionation. Measured Pb isotopic ratios were corrected for instrumental mass fractionation of 1.2‰ per atomic mass unit by reference to repeated analyses of the NIST 981 Pb standard.
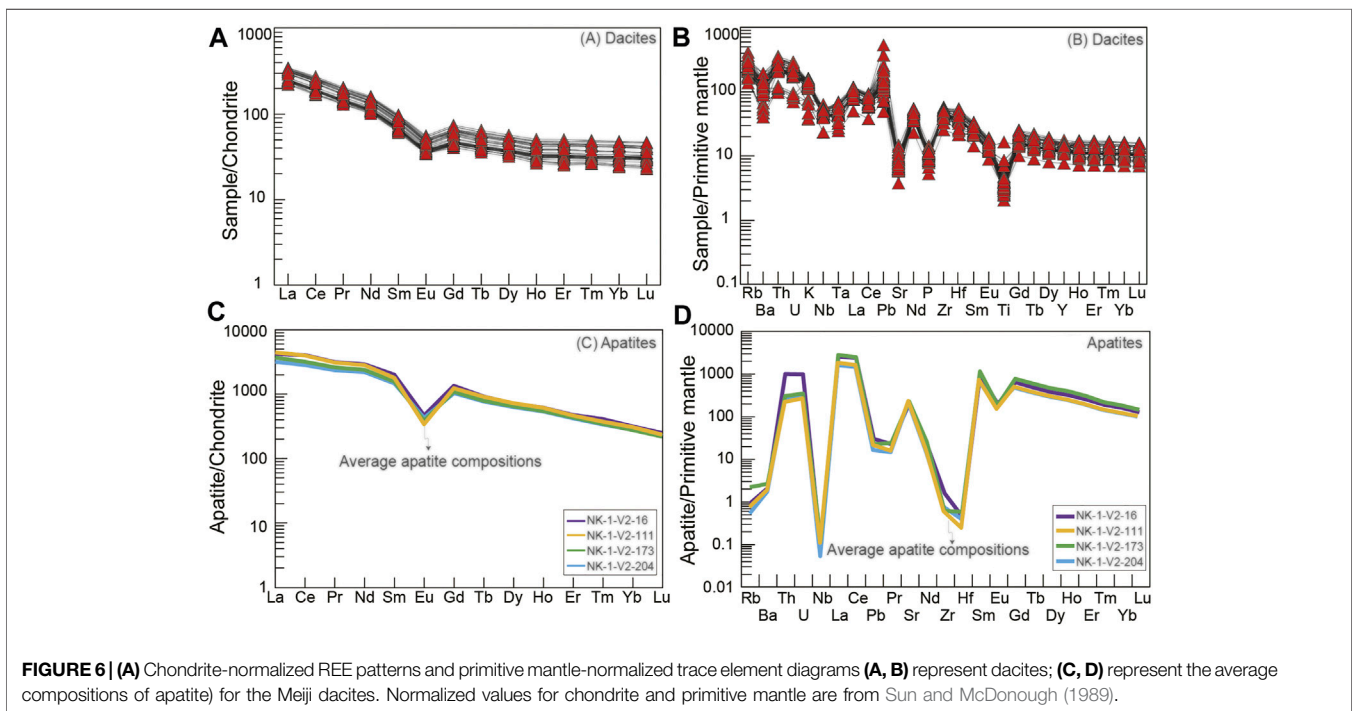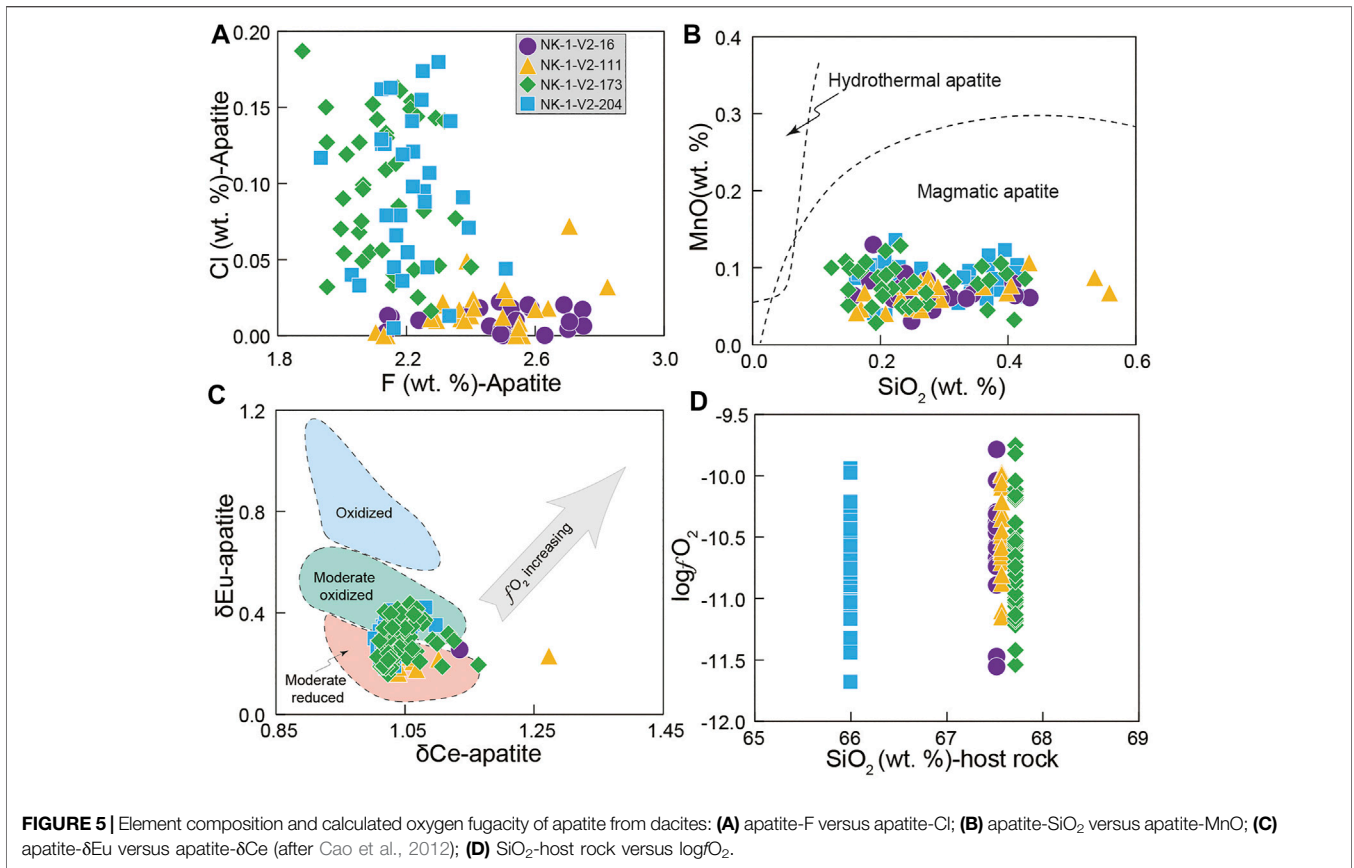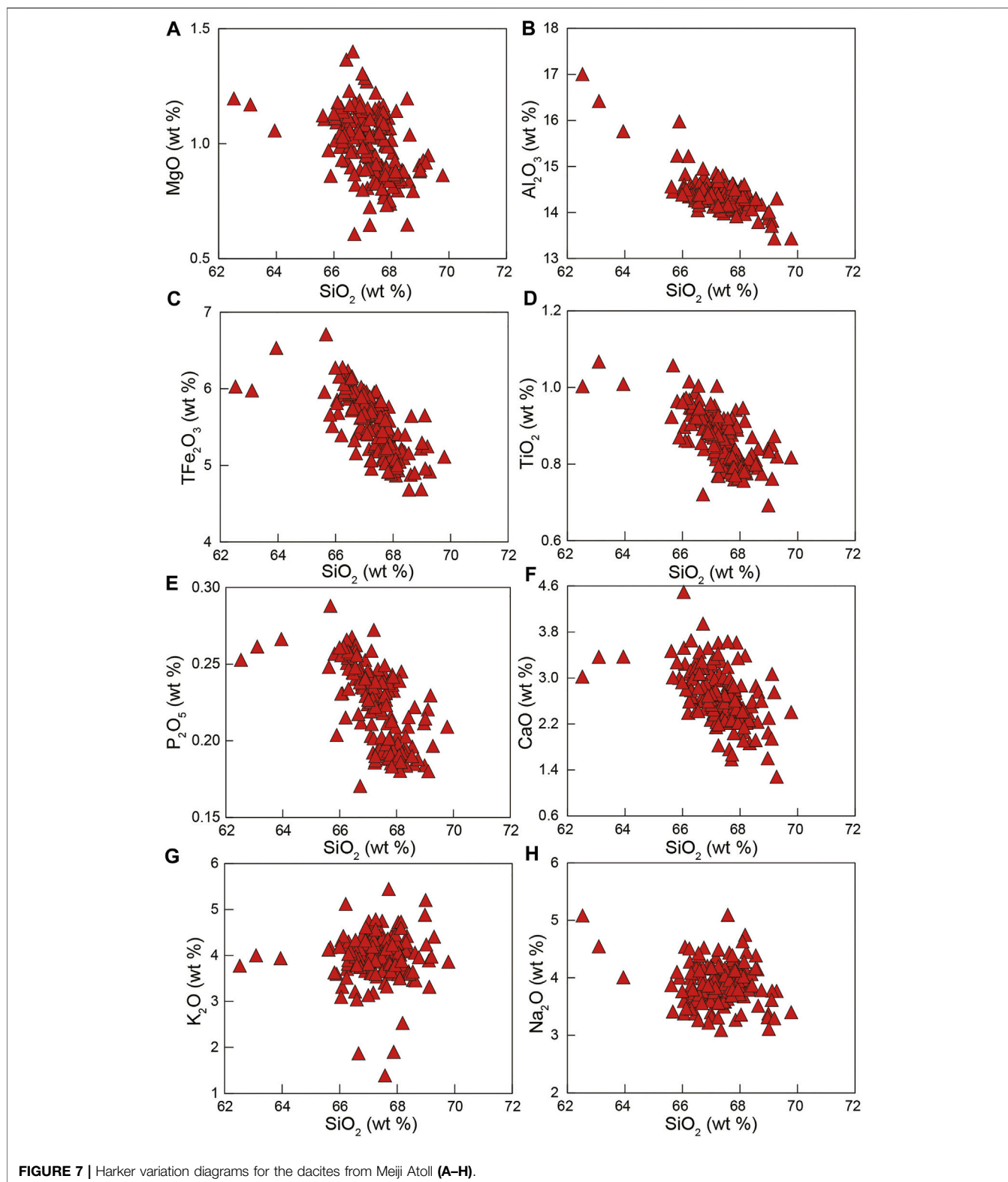
RESULTS

Apatite U-Pb Ages

The U-Pb isotopes of apatite are listed in **Supplementary Table S1**. Apatite grains from the Meiji dacites are mostly euhedral to subhedral in morphology, and transparent to light brown in color. BSE images show that some of them are characterized by core-rim zonation textures and contain cracks filled with mineral inclusions like calcite (**Figure 4D**). They have widths of 25–320 μm and length to width ratios of 1:1–4:1 in the thin sections. The U-Pb isotope data plot nearly along linear arrays in Tera-Wasserburg diagrams (**Figure 4**), with lower intercept ages of 232 ± 15 Ma (MSWD = 0.18, n = 24) for sample NK-1-V2-16, 216 ± 13 Ma (MSWD = 1.7, n = 52) for sample NK-1-V2-173, and 225 ± 11 Ma (MSWD = 0.38, n = 47) for sample NK-1-V2-204 (**Supplementary Table S1**). The ^{207}Pb-corrected weighted mean ^{206}Pb/^{238}U ages are 215.6 ± 9.6 Ma (MSWD = 0.23, n = 24) for sample NK-1-V2-16, 204.7 ± 5.3 Ma (MSWD = 0.77, n = 52) for sample NK-1-V2-173, and 221.1 ± 5.3 Ma (MSWD = 0.35, n = 47) for sample NK-1-V2-204 (**Figure 4**).
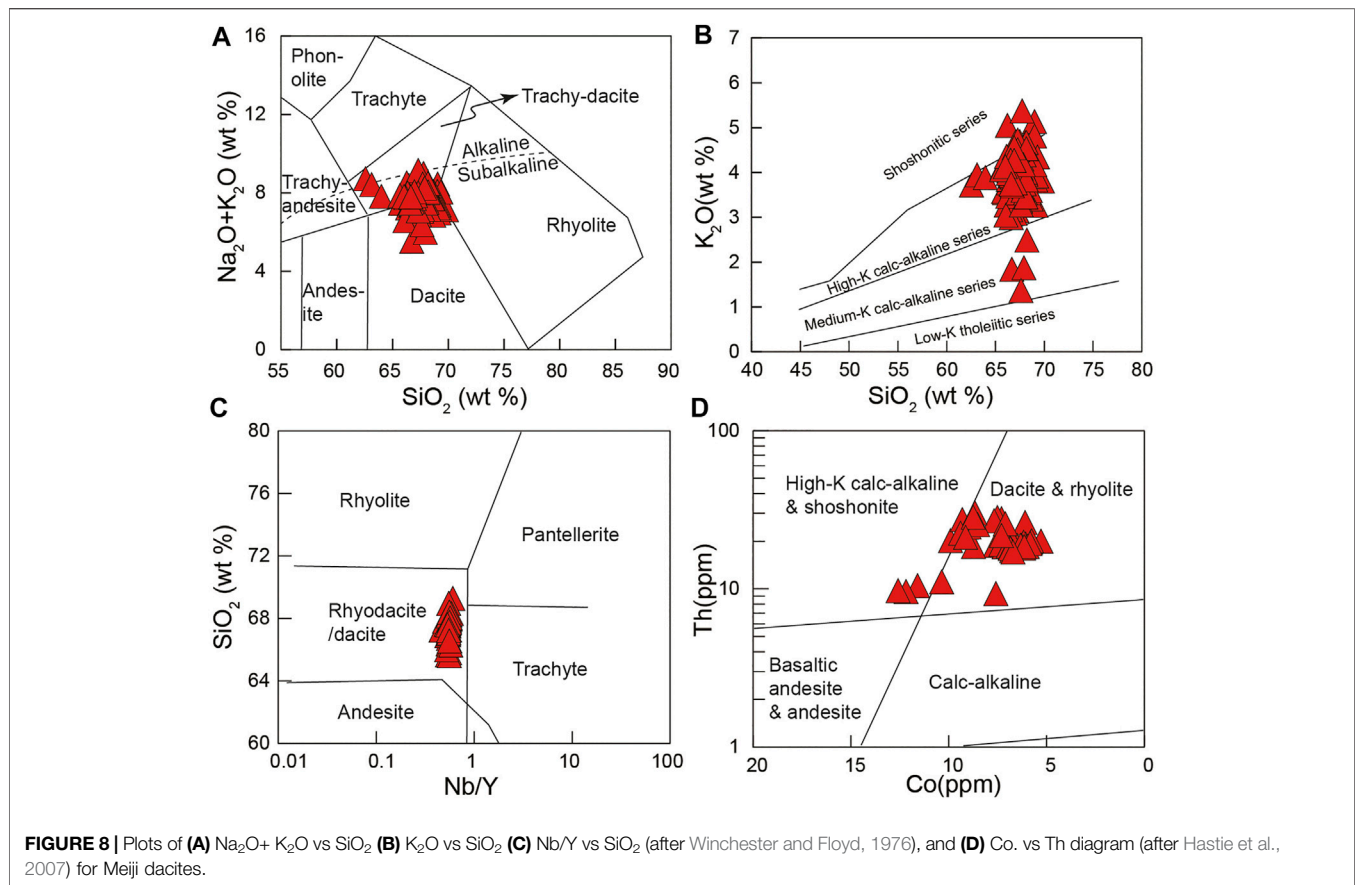
Apatite Compositions

Major and trace elements of apatite are listed in **Supplementary Tables S2, S3**, respectively. Apatite from different samples contains <1.0 wt% Al$_2$O$_3$ and show limited variations in both CaO and P$_2$O$_5$, i.e., 50.6–54.6 wt% and 41.9–45.3 wt%,

FIGURE 5 | Element composition and calculated oxygen fugacity of apatite from dacites: **(A)** apatite-F versus apatite-Cl; **(B)** apatite-SiO_2 versus apatite-MnO; **(C)** apatite-δEu versus apatite-δCe (after Cao et al., 2012); **(D)** SiO_2-host rock versus logfO_2.

FIGURE 6 | (A) Chondrite-normalized REE patterns and primitive mantle-normalized trace element diagrams **(A, B)** represent dacites; **(C, D)** represent the average compositions of apatite) for the Meiji dacites. Normalized values for chondrite and primitive mantle are from Sun and McDonough (1989).

FIGURE 7 | Harker variation diagrams for the dacites from Meiji Atoll **(A–H)**.

respectively. Most apatite from the Meiji dacites is fluorapatite, containing 1.9–2.8 wt% F and <0.2 wt% Cl, which is typical of igneous apatite (Chu et al., 2009). A rough negative correlation exists between F and Cl contents (**Figure 5A**). In the SiO_2 vs MnO

diagram (**Figure 5B**), all apatite data plot within the field of magmatic apatite. The Meiji dacites apatite grains contain 1.7–26.7 ppm U, 5.5–110 ppm Th, 88–454 ppm Sr, and 273–2,441 ppm Y. They show consistent trace element

FIGURE 8 | Plots of (A) $Na_2O+ K_2O$ vs SiO_2 (B) K_2O vs SiO_2 (C) Nb/Y vs SiO_2 (after Winchester and Floyd, 1976), and (D) Co. vs Th diagram (after Hastie et al., 2007) for Meiji dacites.

patterns (**Figure 6**), are slightly enriched in LREE relative to HREE with $(Ce/Yb)_N$ of 9–18, and display notable negative anomalies in Eu, Nb, Hf, Ba, and Zr.
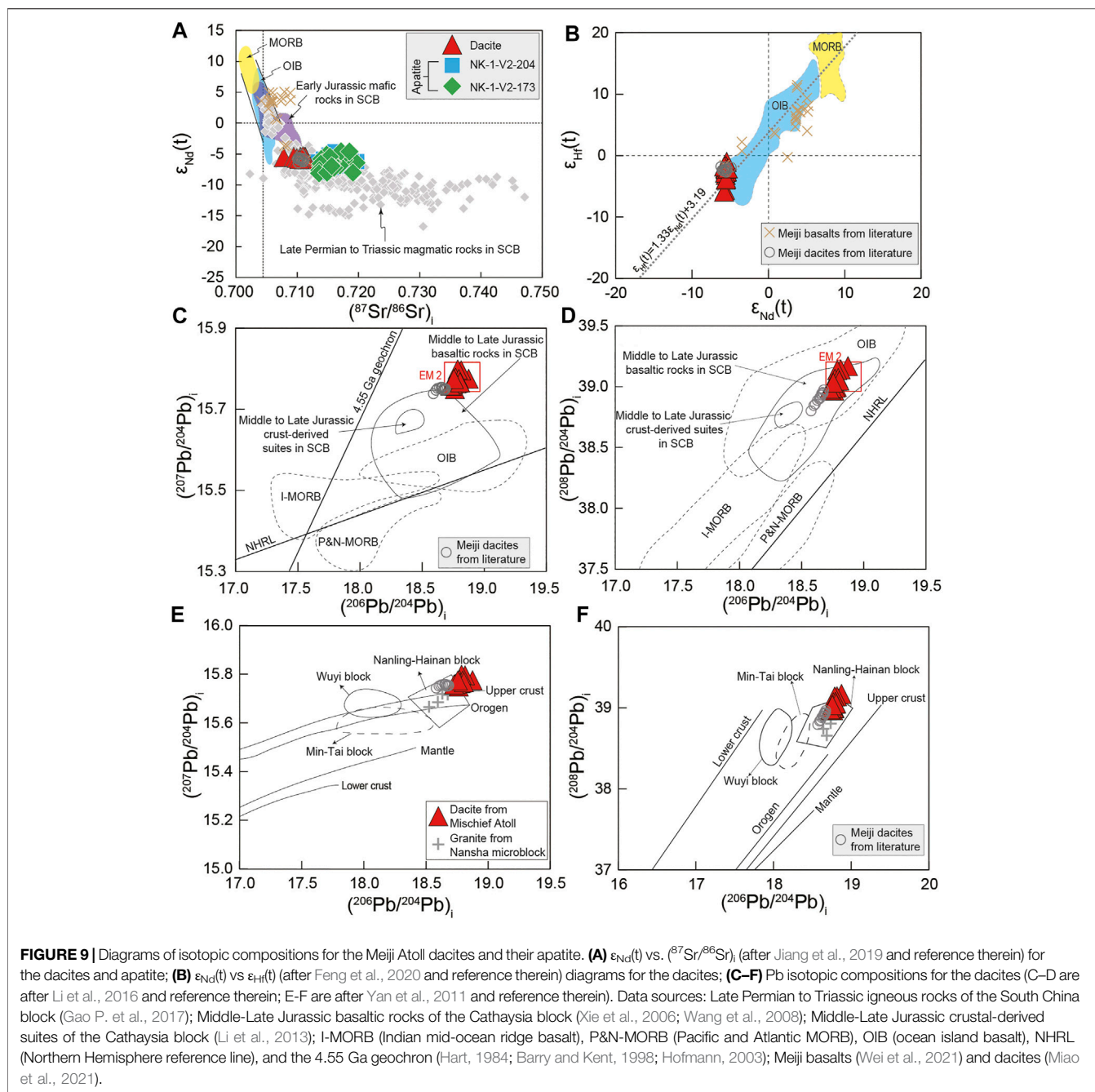
In-situ Sr-Nd isotopes have only obtained for apatite from two samples (NK-1-V2-173 and NK-1-V2-204), as those grains from the other two samples (NK-1-V2-16 and NK-1-V2-111) were not big enough for laser ablation analysis. The Sr-Nd isotopes are listed in **Supplementary Table S4**, where the initial $^{87}Sr/^{86}Sr$ ratios and $\varepsilon_{Nd}(t)$ values were calculated using the obtained U-Pb ages. The results show that the apatite has considerable variation in both $^{87}Rb/^{86}Sr$ and $^{87}Sr/^{86}Sr$ ratios (**Supplementary Table S4**), with respective ranges of 0.0005–0.4699 and 0.71293–0.72006, yielding $(^{87}Sr/^{86}Sr)_i$ ratios of 0.71289–0.71968. In contrast, the apatite has relatively homogeneous $^{147}Sm/^{144}Nd$ (0.1232–0.1359) and $^{143}Nd/^{144}Nd$ (0.512,134–0.512,313) ratios, yielding $\varepsilon_{Nd}(t)$ values of -8.1 ~ -4.6 and two-stage Nd model ages of 1,365–1,639 Ma.

Whole-Rock Compositions

Whole rock major and trace elements of the Meiji dacites are listed in **Supplementary Table S5**. Overall, they are relatively fresh, as indicated by their low loss on ignition (LOI) values (<1.5 wt%). Whole rock major elements were recalculated to 100% on an anhydrous basis. The Meiji dacites contain 62.53–69.78% SiO_2, 0.61–1.68% MgO, 4.68–6.71% Fe_2O_3, 13.43–17.01% Al_2O_3, and 1.28–5.49% CaO, giving Mg# values

$[= 100×Mg/(Mg + Fe^{2+})]$ of 21–43. Their SiO_2 contents negatively correlate with MgO, Al_2O_3, Fe_2O_3, TiO_2, P_2O_5, and CaO (**Figures 7A–F**), but not with K_2O nor Na_2O (**Figures 7G,H**). They have total alkali contents $(Na_2O+ K_2O)$ of 5.63–9.28 wt%. The Meiji dacites belong to the subalkaline series and plot within the fields of dacites and trachydacites in the TAS (total alkali-silica) diagram (**Figure 8A**). They are highly variable in K_2O contents (**Figure 8B**), most of which plot within the field of the high-K calc-alkaline series. The Meiji dacites plot entirely within the field of rhyodacite/dacite in the SiO_2-Nb/Y diagram (**Figure 8C**), and in the field of dacite and rhyolite in the Th-Co diagram (**Figure 8D**). They show enriched patterns in LREE and relatively flat patters in both MREE and HREE (**Figure 6A**), with $(Ce/Yb)_N$ of 1.3–7.4. They also display enrichment in large ion lithophile elements (LILE; e.g., Rb, Ba, Th, U), and negative anomalies in high field strength elements (HFSE; e.g., Nb, Ta, Ti), Eu, and Sr (**Figure 6B**).

Whole rock Sr-Nd-Hf-Pb isotopes of the Meiji dacites are shown in **Supplementary Table S6**. They have enriched Sr-Nd-Hf isotopic characteristics (**Figure 9A–C**), with initial $^{87}Sr/^{86}Sr$ ratios of 0.7078–0.7164, $\varepsilon_{Nd}(t)$ values of -5.8 ~ -5.3, and $\varepsilon_{Hf}(t)$ values of -5.8 ~ -1.0. The dacite has similar $^{143}Nd/^{144}Nd$ ratios with its apatite, but less radiogenic $^{87}Sr/^{86}Sr$ ratios than apatite (**Figure 12A**). They also show the similar Sr-Nd isotopic compositions to the Late Permian to Triassic igneous rocks in the SCB (Gao P. et al., 2017). The calculated two-stage Nd model

FIGURE 9 | Diagrams of isotopic compositions for the Meiji Atoll dacites and their apatite. **(A)** $\varepsilon_{Nd}(t)$ vs. $(^{87}Sr/^{86}Sr)_i$ (after Jiang et al., 2019 and reference therein) for the dacites and apatite; **(B)** $\varepsilon_{Nd}(t)$ vs $\varepsilon_{Hf}(t)$ (after Feng et al., 2020 and reference therein) diagrams for the dacites; **(C–F)** Pb isotopic compositions for the dacites (C–D are after Li et al., 2016 and reference therein; E–F are after Yan et al., 2011 and reference therein). Data sources: Late Permian to Triassic igneous rocks of the South China block (Gao P. et al., 2017); Middle-Late Jurassic basaltic rocks of the Cathaysia block (Xie et al., 2006; Wang et al., 2008); Middle-Late Jurassic crustal-derived suites of the Cathaysia block (Li et al., 2013); I-MORB (Indian mid-ocean ridge basalt), P&N-MORB (Pacific and Atlantic MORB), OIB (ocean island basalt), NHRL (Northern Hemisphere reference line), and the 4.55 Ga geochron (Hart, 1984; Barry and Kent, 1998; Hofmann, 2003); Meiji basalts (Wei et al., 2021) and dacites (Miao et al., 2021).

ages vary from 1,495 to 1,395 Ma and the two-stage Hf isotope model ages vary from 1,534 to 1,122 Ma. In the $\varepsilon_{Hf}(t)$-$\varepsilon_{Nd}(t)$ diagram (**Figure 12B**), the dacites data plot along the terrestrial array, i.e., $\varepsilon_{Hf}(t) = 1.33 \times \varepsilon_{Nd}(t) + 3.19$ (Vervoort et al., 2011), without significant Nd-Hf isotopic decoupling. The dacites have consistent Pb isotopic compositions (**Figures 12C–F**) with $(^{206}Pb/^{204}Pb)_i$ ratios of 18.73–18.87 $(^{207}Pb/^{204}Pb)_i$ ratios of 15.75–15.80, and $(^{208}Pb/^{204}Pb)_i$ ratios of 38.97–39.17. In the $^{207}Pb/^{204}Pb$-$^{206}Pb/^{204}Pb$ diagram (**Figure 12C**), the Meiji dacites plot to the right of the 4.55 Ga geochron line, and notably above the North Hemisphere reference line (NHRL).

The Meiji dacites have Pb isotopes similar to Mesozoic granites dredged from the Nansha microblock (**Figures 12C–F**).

DISCUSSION

Timing of the Volcanism of Meiji Atoll

The U-Pb dating of apatite separated from three Meiji dacites samples yielded Triassic ages of ca. 221–205 Ma (**Figure 4**), which are identical within uncertainties to the SIMS U-Pb ages (ca. 218 Ma) previously reported for zircons separated from the Meiji

dacites (Miao et al., 2021; Wei et al., 2021). Thus, geochronological results of apatite and zircon jointly corroborate the existence of Triassic magmatism on Meiji Atoll. As the basalts are interbedded with dacites throughout the core, we infer that both lithologies erupted coevally, which is consistent with the lack of chilled margins. The U-Pb ages obtained by both apatite and zircon collected at 1,197.20–1,502.05 mbsf are identical to the whole rock $^{40}Ar/^{39}Ar$ ages and U-Pb ages of zircons collected at 1,485–1,705 mbsf within uncertainties (Miao et al., 2021; Wei et al., 2021), also indicating coeval eruption of the Meiji dacites. The identical U-Pb ages indicate that the U-Pb isotope system of apatite was not disturbed during low temperature alteration. Furthermore, this also suggests that most of the dacites experienced fast post-magmatic cooling to below ~450 °C. Paleomagnetism has demonstrated southward drift of the Meiji volcanic rocks after their eruption (Wei et al., 2021). Therefore, Meiji Atoll was originally part of the continental arc along the coastal region of the SCB related to Paleo-Pacific (Panthalassa) subduction during the Triassic.

Magmatic Processes Recorded by Apatite

Apatite is a very common accessory mineral in most igneous and metamorphic rocks, and can host various trace elements, including REEs and other important trace elements such as Sr and V (Prowatke and Klemme, 2006), through substitution in the crystal lattice (Hughes and Rakovan, 2015; O'Sullivan et al., 2020). Therefore, apatite has the capacity to retain geochemical information about the host magma through the course of magmatic evolution (Chu et al., 2009), and thus can provide effective constraints on compositions and original tectonic settings of their parental magmas (Miles et al., 2013; Miles et al., 2014; Pan et al., 2016; Zhang et al., 2020; Zhang et al., 2021). Previous studies have shown that the evolution of the silicic magmas is potentially recorded by the Eu anomaly, Sr content, and REE pattern of apatite (Zafar et al., 2020).

Apatite commonly occurs as euhedral phenocrysts in the Meiji dacites (**Figure 3A**), or as needle-shaped inclusions within plagioclase (**Figure 3B**). Such textures indicate its magmatic origin, and also suggest that it crystallized earlier than plagioclase. A magmatic origin for apatite in the Meiji dacites is supported by its major element compositions, where all analyzed apatite grains plot within the field of magmatic apatite in the SiO_2-MnO diagram (**Figure 5B**). It has been suggested that trace element compositions of apatite are strongly dependent on the compositions of their host magmas, and also related to the timing of their crystallization relative to other minerals (e.g., plagioclase and titanite). Apatite in the Meiji dacites show LREE-enriched patterns and a strongly negative Eu anomaly (**Figure 6C**). Such a pronounced negative Eu anomaly is a common feature of apatite from granitoids, which has been ascribed to earlier crystallization of plagioclase than apatite. This is because Eu^{2+} is more compatible than the other REE^{3+} ions in plagioclase and its crystallization would result in depletion of Eu in the host magmas (Zafar et al., 2020). But such an explanation is precluded here because microtextures suggest an earlier crystallization of apatite relative to plagioclase in the Meiji
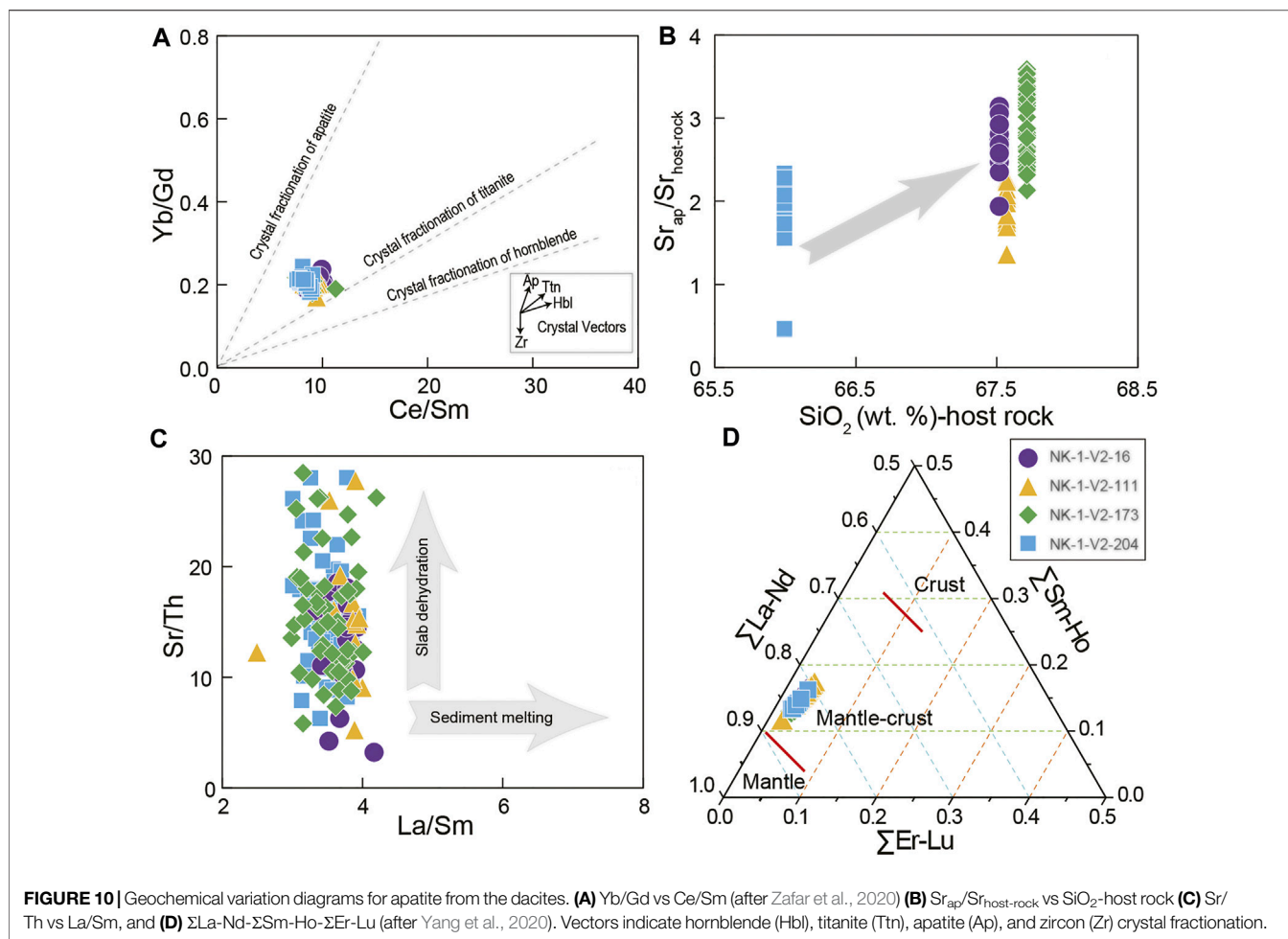
dacites (**Figure 3B**). Moreover, earlier crystallization of apatite relative to feldspar is also supported by a positive correlation between $Sr_{apatite}/Sr_{host-rock}$ values and whole rock SiO_2 contents (**Figure 10B**). Therefore, it is most plausible that the negative Eu anomaly in apatite of the Meiji dacites was inherited from their host magmas and their source materials. This implies that plagioclase was a residual mineral phase in the source materials of the Meiji dacites (Yu et al., 2019).

Trace elements of apatite can also be utilized to trace the fractionation of other minerals during magmatic evolution because such minerals tend to compete with apatite for trace elements (e.g., REEs; Miles et al., 2013). In the Ce/Sm-Yb/Gd diagram (**Figure 10A**), the Meiji dacites plot along the trend of titanite fractionation, suggesting that titanite crystallized from the host magma together with apatite. Crystallization of titanite with apatite is also consistent with the BSE image showing mineral association of titanite and apatite (**Figure 3C**) and negative correlations between the Sr content and LREE ratios, e.g., $(La/Yb)_N$ $(La/Sm)_N$, and $(Sm/Yb)_N$ (**Figure 11D**). This is because crystallization of titanite can cause a strong depletion in LREE and mild depletion in Sr in coexisting apatite (Chu et al., 2009). It has been suggested that apatite generally incorporates less Sr than its host magma (Chu et al., 2009), whereas apatite from the Meiji dacites has much higher Sr contents than its host rock: 88–454 ppm (average = 372 ppm) vs 125–183 ppm (average = 158 ppm), respectively. Such a difference might suggest earlier fractionation of plagioclase than apatite, but that would contradict the microtextures. Alternatively, higher Sr contents in apatite than its host rock can be explained by the involvement of mafic magmas (Chu et al., 2009). Such a model is consistent with the fact that apatite of the Meiji dacites exhibits variable core-rim zonation textures (**Figure 4D**) and plots entirely within the field of mixing between mantle- and crust-derived magmas (**Figure 10D**). Apatite in the Meiji dacites is also characterized by high Ce/Pb ratios, low Th/U ratios (**Figure 9D**) and cracks filled with mineral inclusions like calcite (**Figure 4D**), suggesting the involvement of fluids in their formation (Yang et al., 2020). The fluids should be F-rich, as apatite in the Meiji dacites has much higher contents of F than Cl, i.e., belonging to fluorapatites.

Trace elements (e.g., Ce, Eu, and Mn) in apatite are also sensitive to the oxygen fugacity (fO_2) of the host magmas and thus can provide effective constraints on the redox state of magmas (Miles et al., 2014). Quantitative relationship between the magmatic oxygen fugacity (fO_2) of silicic magmas and the Mn concentration of apatite has been experimentally calibrated (Miles et al., 2014), i.e., $logfO_2 = -0.0022$ (±0.0003)Mn (ppm)−9.75 (±0.46). The calculated results show that apatite from the studied Meiji dacites have similar ranges of $logfO_2$ values (**Figure 5D**), -11.68 ~ -9.75, indicating moderate reduced to oxidized states. This is consistent with both negative Eu and Ce anomalies displayed by apatite of the Meiji dacites (**Figure 5C**).

Petrogenesis of the Meiji Atoll Dacites

Although the Meiji dacites were drilled from depths below the seafloor, they are quite fresh and have low LOI values (<1.5 wt%), suggesting a very low degree of alteration. Moreover, their major elements show no correlation with LOI values, further suggesting

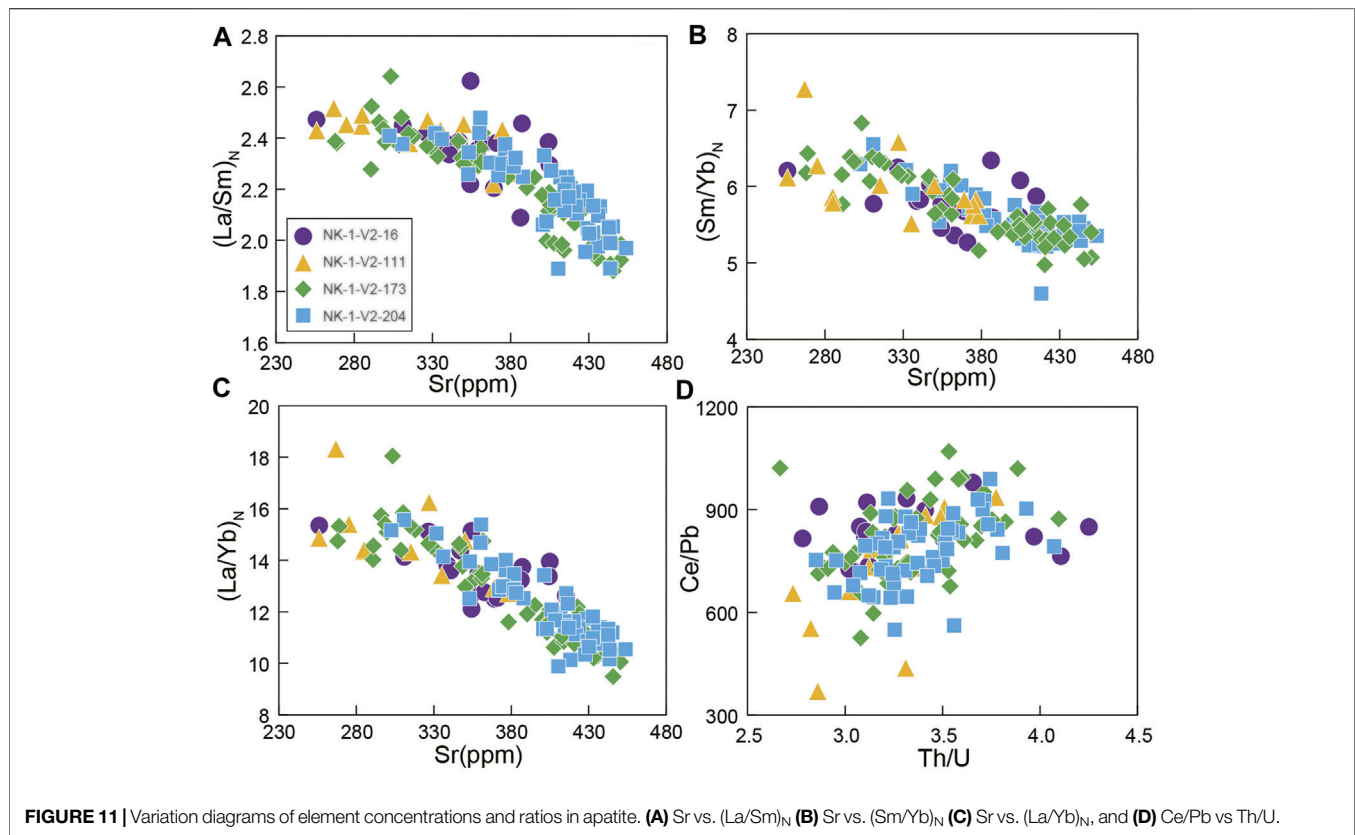**FIGURE 10 |** Geochemical variation diagrams for apatite from the dacites. **(A)** Yb/Gd vs Ce/Sm (after Zafar et al., 2020) **(B)** $Sr_{ap}/Sr_{host-rock}$ vs SiO_2-host rock **(C)** Sr/Th vs La/Sm, and **(D)** ΣLa-Nd-ΣSm-Ho-ΣEr-Lu (after Yang et al., 2020). Vectors indicate hornblende (Hbl), titanite (Ttn), apatite (Ap), and zircon (Zr) crystal fractionation.

negligible alteration. Strong correlations exist among the immobile elements, such as HFSEs (e.g., Zr, Hf, Nb, and Ta) and REEs. These elements are utilized to decipher the petrogenetic processes and constrain the source features of the Meiji dacites.

Previous studies have proposed various mechanisms for the formation of dacites in non-ridge settings, including crustal melting (Borg and Clynne, 1998), fractionation of mafic magmas (Yamamoto, 2007), and assimilation of crustal materials into mantle-derived magmas (Crabtree and Lange, 2010; Frey and Lange, 2011). The Meiji dacites are calc-alkaline in composition, mostly plotting within the high-K calc-alkaline field (**Figure 8B**). They are characterized by high contents of SiO_2 and K_2O, but low concentrations of MgO, Fe_2O_3, CaO, Cr, and Ni. These features rule out the possibility that they were generated through hydrous mantle melting. Throughout the whole NK-1 core, dacites are volumetrically dominant over basalts (**Figure 2A**). This suggests that the Meiji dacites were unlikely to have been produced through fractionation of mafic magmas. Moreover, there is a clear compositional gap between the basalts and dacites (Wei et al., 2021), which also argues against the fractionation of mafic magmas. Intermediate lithologies with continuous variations in compositions would be expected, but are not observed.

Apatite in granitoids commonly contains less Sr than its whole rock composition, which stands in stark contrast to the Meiji dacite and its apatite. It has been suggested that involvement of mafic magmas in the parental magma can result in higher Sr contents in apatite than its host magmas (Chu et al., 2009). Apatite in the Meiji dacite has $(^{87}Sr/^{86}Sr)_i$ ratios more radiogenic than its host rock (**Figure 12A**). This suggests that Meiji apatite crystallized from parental magmas with $(^{87}Sr/^{86}Sr)_i$ ratios higher than its host dacite, and therefore a component, probably of mafic magma, with lower $(^{87}Sr/^{86}Sr)_i$ ratios was added after the crystallization of apatite. In the ternary diagram of REE (**Figure 10D**), all apatite in the Meiji dacite plots within the field of crust-mantle mixing, which favors the addition of mafic magmas. Nevertheless, neither mafic microgranular enclaves (MMEs) nor quartz ocelli rimmed by hornblende and/or biotite was observed in the Meiji dacites throughout the core. This argues against the addition of significant amounts of mafic magma to the parental magma of the Meiji dacites (Perugini and Poli, 2012).

In a previous study (Wei et al., 2021), we have proposed that Meiji Atoll was part of the continental magmatic arc of the SCB, which was rifted and drifted southward to its current position. In such a scenario, the Meiji dacites might be products of magmas

FIGURE 11 | Variation diagrams of element concentrations and ratios in apatite. **(A)** Sr vs. $(La/Sm)_N$ **(B)** Sr vs. $(Sm/Yb)_N$ **(C)** Sr vs. $(La/Yb)_N$, and **(D)** Ce/Pb vs Th/U.
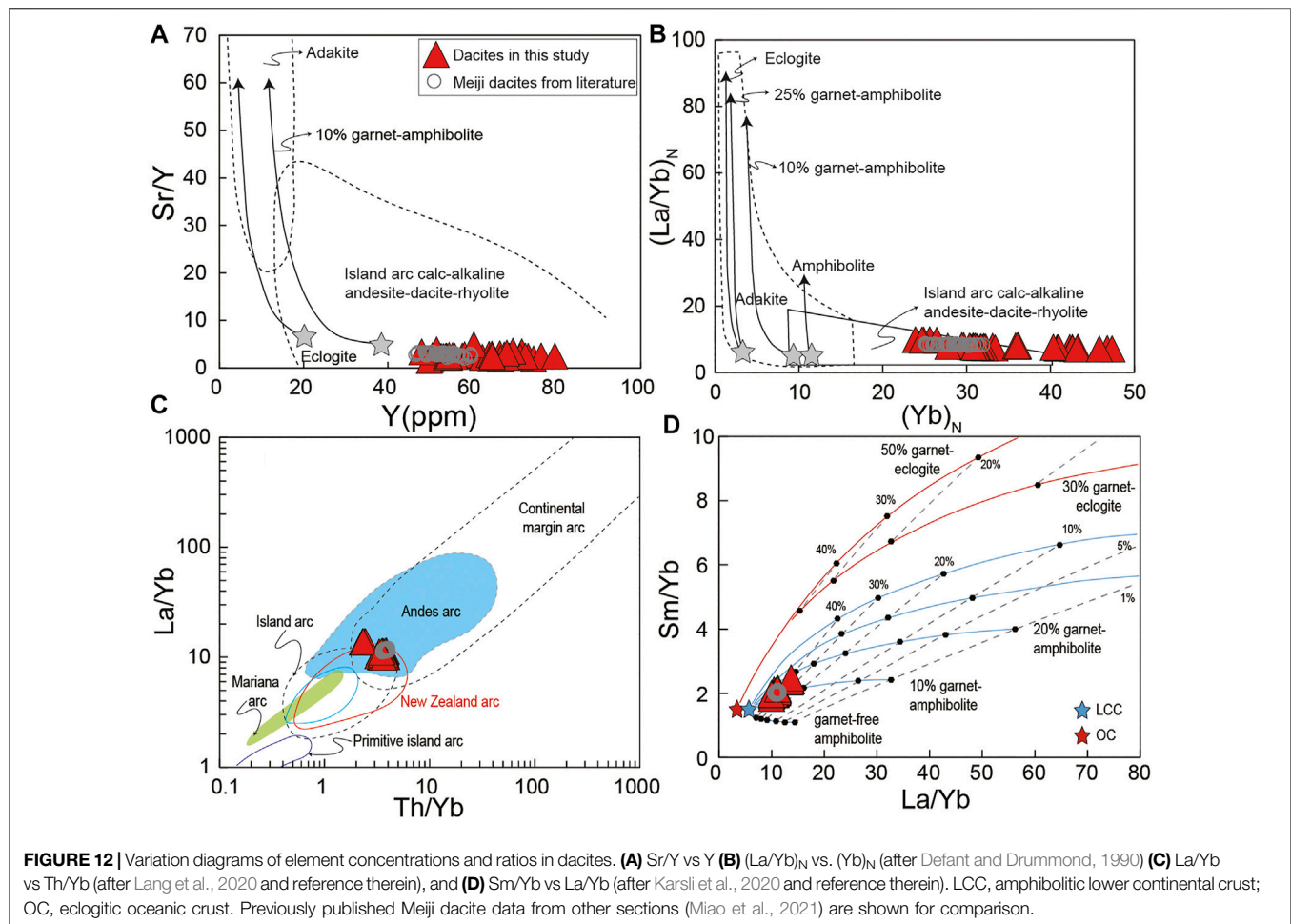
derived from the lower continental crust beneath the SCB. Modeling using whole Sm/Yb and La/Yb ratios (Karsli et al., 2020) suggests that the Meiji dacites can be produced by <40% partial melting of amphibolites containing ~10% garnet in the lower continental crust (**Figure 12A, B**). On the other hand, the Meiji dacites are compositionally different from adakites produced by partial melting of a subducted slab (Defant and Drummond, 1990) or thickened lower crust (Ma et al., 2016). They have high Y and Yb contents, but low Sr contents, yielding very low Sr/Y and La/Yb ratios; they thus plot entirely out of the fields defined by adakites (**Figures 11A,B**). This suggests that melting was not occurred at the base of thickened lower continental crust beneath the SCB during Paleo-Pacific (Panthalassa) subduction during the Late Triassic.

Formation of the Meiji dacites through melting of the lower continental crust beneath the SCB is also supported by their isotopic compositions. The Sr-Nd-Pb isotopes of the Meiji dacites show affinities with the Mesozoic igneous rocks of the SCB (**Figure 12**; Wang et al., 2008; Li et al., 2013). Both Nd and Hf isotopes of the Meiji dacites yield similar two-stage model ages of 1.5–1.1 Ga, which are relatively younger than the age of the metamorphic basement beneath the Cathaysia block (>1.85 Ga; Xu et al., 2007). Such a difference requires accretion of juvenile crust during the Mesoproterozoic, plausibly through magmatic underplating, which might be evidenced in the Mesoproterozoic (1,441–1,424 Ma) mafic rocks with depleted Hf-Nd isotopes ($\varepsilon_{Nd}(t)$ of +5.5~+5.9 and $\varepsilon_{Hf}(t)$ of +10.3~+12.4) of Hainan Island (Zhang L. et al., 2018).

The existence of Mesoproterozoic basement in the SCB is also supported by the Nd model ages (1776–928 Ma) of the Jurassic (159–127 Ma) granitic rocks dredged from the Nansha micro-block (Yan et al., 2010). Moreover, multichannel seismic reflection studies reveal a layer with high velocity in the lower crust extending southwards from the northeastern margin of the SCS to the conjugate southern margin, which might represent the underplated mafic magmas (Zhao et al., 2010; Peng et al., 2020).

Tectonic Implications

Consistent with previous zircon U-Pb geochronological studies (Miao et al., 2021; Wei et al., 2021), apatite U-Pb ages also confirm the formation of the Meiji dacites during the Late Triassic. Basalts interbedded with the dacites throughout the NK-1 core drilled on Meiji Atoll show subduction-related geochemical compositions, which were generated through partial melting of the mantle wedge that was metasomatized by agents released from the subducted Paleo-Pacific plate (Wei et al., 2021). Underplating of the mafic magma triggered the melting of the lower continental crust, giving rise to the dacites. Therefore, the Meiji volcanic rocks were generated in a Triassic subduction zone. Paleomagnetic data suggest that the Meiji volcanic rocks were erupted at ~16.2° N, thus Meiji Atoll has experienced a 4.1° ± 1.5° post-eruption southward drift relative to the SCB (Wei et al., 2021). Therefore, Meiji Atoll originally occupied part of the continental magmatic arc developed along the SCB as a result of Paleo-Pacific (Panthalassa)

FIGURE 12 | Variation diagrams of element concentrations and ratios in dacites. **(A)** Sr/Y vs Y **(B)** (La/Yb)$_N$ vs. (Yb)$_N$ (after Defant and Drummond, 1990) **(C)** La/Yb vs Th/Yb (after Lang et al., 2020 and reference therein), and **(D)** Sm/Yb vs La/Yb (after Karsli et al., 2020 and reference therein). LCC, amphibolitic lower continental crust; OC, eclogitic oceanic crust. Previously published Meiji dacite data from other sections (Miao et al., 2021) are shown for comparison.

subduction, and was rifted from the SCB and drifted to the south due to the opening of the SCS.

The Meiji dacites provide supportive evidence for the existence of a Triassic Andean-type active continental margin in the SCB related to Paleo-Pacific subduction, which is also consistent with the discovery of a Cretaceous arc record beneath the northwestern SCS (Cui et al., 2021). Continental extension and seafloor spreading in this region resulted in the rifting and southward drifting of different microblocks as Triassic magmatism has also been discovered in southeast Asia (e.g., Borneo) that formed during subduction of the Paleo-Pacific lithosphere (Breitfeld et al., 2017). Therefore, Meiji Atoll and other microblocks in the SCS (e.g., Palawan and Mindoro) exemplify the rifting and drifting of microcontinents and reinforces the notion of a "ribbon continent" (Celâl Şengör, 1984). A portion of the rifted ribbons has been accreted to the western margin of the Philippine sea plate and become the basement under the Luzon arc (Shao et al., 2015). The ribbon continents might also play a key role in accretionary orogens throughout the geological record, e.g., the Central Asian Orogenic Belt (Jahn, 2004) and the eastern Tethys (Chung et al., 2013).

CONCLUSION

Consistent with previous zircon U-Pb ages, apatite U-Pb dating supports a Late Triassic (221–204 Ma) age for dacites drilled from Meiji Atoll. The Meiji dacites show arc-related geochemical features, but no affinity to adakites. Trace element modeling suggests that the Meiji dacites can be generated by <40% partial melting of amphibolites containing ~10% garnet. Therefore, the Meiji dacites were produced by partial melting of the lower continental crust beneath the SCB, which was probably triggered by the underplating of mafic magmas as a response to Paleo-Pacific (Panthalassa) subduction during the Triassic. The Meiji Atoll, together with other microblocks in the SCS, were rifted from the SCB and drifted southward due to continental extension and the opening of the SCS.

DATA AVAILABILITY STATEMENT

The original contributions presented in the study are included in the article/**Supplementary Material**, further inquiries can be directed to the corresponding author.

AUTHOR CONTRIBUTIONS

FUNDING

ACKNOWLEDGMENTS

SUPPLEMENTARY MATERIAL

The Supplementary Material for this article can be found online at: https://www.frontiersin.org/articles/10.3389/feart.2021.780007/full#supplementary-material

REFERENCES

Barckhausen, U., Engels, M., Franke, D., Ladage, S., and Pubellier, M. (2014). Evolution of the South China Sea: Revised Ages for Breakup and Seafloor Spreading. *Mar. Pet. Geol.* 58, 599–611. doi:10.1016/j.marpetgeo.2014.02.022

Barry, T. L., and Kent, R. W. (1998). "Cenozoic Magmatism in Mongolia and the Origin of central and East Asian Basalts," in *Mantle Dynamics and Plate Interactions in East Asia*. Editors M. F. J. Flower, S. L. Chung, C. H. Lo, and T. Y. Lee (Washington, D. C: American Geophysical Union), 347–364. AUG. doi:10.1029/gd027p0347

Bing-Quan, Z., Hui-Fen, W., Yu-Wei, C., Xian-Yang, C., Yao-Guo, H., and Jin, X. (2004). Geochronological and Geochemical Constraint on the Cenozoic Extension of Cathaysian Lithosphere and Tectonic Evolution of the Border Sea Basins in East Asia. *J. Asian Earth Sci.* 24 (2), 163–175. doi:10.1016/j.jseaes.2003.10.006

Borg, L. E., and Clynne, M. A. (1998). The Petrogenesis of Felsic Calc-Alkaline Magmas from the Southernmost Cascades, California: Origin by Partial Melting of Basaltic Lower Crust. *J. Petrol.* 39, 1197–1222. doi:10.1093/petroj/39.6.1197

Breitfeld, H. T., Hall, R., Galin, T., Forster, M. A., and Boudagher-Fadel, M. K. (2017). A Triassic to Cretaceous Sundaland-Pacific Subduction Margin in West Sarawak, Borneo. *Tectonophysics* 694, 35–56. doi:10.1016/j.tecto.2016.11.034

Briais, A., Patriat, P., and Tapponnier, P. (1993). Updated Interpretation of Magnetic Anomalies and Seafloor Spreading Stages in the South China Sea: Implications for the Tertiary Tectonics of Southeast Asia. *J. Geophys. Res.* 98 (B4), 6299–6328. doi:10.1029/92jb02280

Cao, M., Li, G., Qin, K., Seitmuratova, E. Y., and Liu, Y. (2012). Major and Trace Element Characteristics of Apatites in Granitoids from Central Kazakhstan: Implications for Petrogenesis and Mineralization. *Resour. Geol.* 62 (1), 63–83. doi:10.1111/j.1751-3928.2011.00180.x

Celâl Şengör, A. M. (1984). The Cimmeride Orogenic System and the Tectonics of Eurasia. *Geol. Soc. Am. Spec. Paper* 195, 1–74. doi:10.1130/SPE195-p1

Chew, D. M., Petrus, J. A., and Kamber, B. S. (2014). U-Pb LA-ICPMS Dating Using Accessory mineral Standards with Variable Common Pb. *Chem. Geology.* 363, 185–199. doi:10.1016/j.chemgeo.2013.11.006

Chu, M.-F., Wang, K.-L., Griffin, W. L., Chung, S.-L., O'Reilly, S. Y., Pearson, N. J., et al. (2009). Apatite Composition: Tracing Petrogenetic Processes in Transhimalayan Granitoids. *J. Petrol.* 50 (10), 1829–1855. doi:10.1093/petrology/egp054

Chung, S.-L., Chiu, H.-Y., Lee, H.-Y., Shao, W.-Y., Zarrinkoub, M. H., and Wu, F.-Y. (2013). "Asian continental Growth in the Phanerozoic: Zircon Hf Isotopic Constraints from the central Asian to Eastern Tethyan Orogenic Belts," in Proceedings, Geological Society of China and Geological Society of America Joint Meeting, "Roof of the World, Chengdu, China, 17–19 June 2013, 298. doi:10.1130/G19796.1

Clift, P., and Lin, J. (2001). Preferential Mantle Lithospheric Extension under the South China Margin. *Mar. Pet. Geology.* 18 (8), 929–945. doi:10.1016/S0264-8172(01)00037-X

Crabtree, S. M., and Lange, R. A. (2010). Complex Phenocryst Textures and Zoning Patterns in Andesites and Dacites: Evidence of Degassing-Induced Rapid Crystallization? *J. Petrol.* 52, 3–38. doi:10.1093/petrology/egq067

Cui, Y., Shao, L., Li, Z.-X., Zhu, W., Qiao, P., and Zhang, X. (2021). A Mesozoic Andean-type Active continental Margin along Coastal South China: New Geological Records from the Basement of the Northern South China Sea. *Gondwana Res.* 99, 36–52. doi:10.1016/j.gr.2021.06.021

Defant, M. J., and Drummond, M. S. (1990). Derivation of Some Modern Arc Magmas by Melting of Young Subducted Lithosphere. *Nature* 347, 662–665. doi:10.1038/347662a0

Ding, W., Franke, D., Li, J., and Steuer, S. (2013). Seismic Stratigraphy and Tectonic Structure from a Composite Multi-Channel Seismic Profile across the Entire Dangerous Grounds, South China Sea. *Tectonophysics* 582 (582), 162–176. doi:10.1016/j.tecto.2012.09.026

Ding, W., Sun, Z., Dadd, K., Fang, Y., and Li, J. (2018). Structures within the Oceanic Crust of the central South China Sea basin and Their Implications for Oceanic Accretionary Processes. *Earth Planet. Sci. Lett.* 488, 115–125. doi:10.1016/j.epsl.2018.02.011

Ding, W., Sun, Z., Mohn, G., Nirrengarten, M., Tugend, J., Manatschal, G., et al. (2020). Lateral Evolution of the Rift-To-Drift Transition in the South China Sea: Evidence from Multi-Channel Seismic Data and IODP Expeditions 367&368 Drilling Results. *Earth Planet. Sci. Lett.* 531, 115932. doi:10.1016/j.epsl.2019.115932

Fan, C., Xia, S., Cao, J., Zhao, F., and Wan, K. (2020). Seismic Constraints on a Remnant Mesozoic Forearc basin in the Northeastern South China Sea. *Gondwana Res.* doi:10.1016/j.gr.2020.10.006

Feng, Y., Yang, J., Sun, J., and Zhang, J. (2020). Material Records for Mesozoic Destruction of the North China Craton by Subduction of the Paleo-Pacific Slab. *Sci. China Earth Sci.* 63, 690–700. doi:10.1007/s11430-019-9564-4

Franke, D., Savva, D., Pubellier, M., Steuer, S., Mouly, B., Auxietre, J.-L., et al. (2014). The Final Rifting Evolution in the South China Sea. *Mar. Pet. Geology.* 58, 704–720. doi:10.1016/j.marpetgeo.2013.11.020

Frey, H. M., and Lange, R. A. (2011). Phenocryst Complexity in Andesites and Dacites from the Tequila Volcanic Field, Mexico: Resolving the Effects of Degassing vs. Magma Mixing. *Contrib. Mineral. Petrol.* 162 (2), 415–445. doi:10.1007/s00410-010-0604-1

Gao, P., Zheng, Y.-F., and Zhao, Z.-F. (2017a). Triassic Granites in South China: A Geochemical Perspective on Their Characteristics, Petrogenesis, and Tectonic Significance. *Earth-Science Rev.* 173, 266–294. doi:10.1016/j.earscirev.2017.07.016

Gao, W., Wang, Z., and Li, C. (2017b). Triassic Magmatism in the Eastern Part of the South China Block: Geochronological and Petrogenetic Constraints from Indosinian Granites. *Geosci. Front.* 8 (3), 445–456. doi:10.1016/j.gsf.2016.03.003

Griffin, W., Powell, W., Pearson, N. J., and O Reilly, S. (2008). "GLITTER: Data Reduction Software for Laser Ablation ICP-MS," in *Laser Ablation-ICP-MS in the Earth Sciences: Current Practices and Outstanding Issues*. Editor P. Sylvester, 308–311.

Hall, R. (2002). Cenozoic Geological and Plate Tectonic Evolution of SE Asia and the SW Pacific: Computer-Based Reconstructions, Model and Animations. *J. Asian Earth Sci.* 20 (4), 353–431. doi:10.1016/S1367-9120(01)00069-4

Hart, S. R. (1984). A Large-Scale Isotope Anomaly in the Southern Hemisphere Mantle. *Nature* 309 (5971), 753–757. doi:10.1038/309753a0

Hastie, A. R., Kerr, A. C., Pearce, J. A., and Mitchell, S. F. (2007). Classification of Altered Volcanic Island Arc Rocks Using Immobile Trace Elements: Development of the Th-Co Discrimination Diagram. *J. Petrol.* 48 (12), 2341–2357. doi:10.1093/petrology/egm062

Hofmann, A. W. (2003). Sampling Mantle Heterogeneity through Oceanic Basalts: Isotopes and Trace Elements. *Treatise Geochem.* 2, 1–44. doi:10.1016/B0-08-043751-6/02123-X

Holloway, N. H. (1982). North Palawan Block, Philippines--Its Relation to Asian Mainland and Role in Evolution of South China Sea. *Bulletin* 66 (9), 1355–1383. doi:10.1306/03B5A7A5-16D1-11D7-8645000102C1865D

Hughes, J. M., and Rakovan, J. F. (2015). Structurally Robust, Chemically Diverse: Apatite and Apatite Supergroup Minerals. *Elements* 11 (3), 165–170. doi:10.2113/gselements.11.3.165

Hutchison, C. S. (2004). Marginal basin Evolution: the Southern South China Sea. *Mar. Pet. Geology.* 21 (9), 1129–1148. doi:10.1016/j.marpetgeo.2004.07.002

Jahn, B.-M. (2004). "The Central Asian Orogenic Belt and Growth of the continental Crust in the Phanerozoic," in *Aspects of the Tectonic Evolution of China*. Editors J. Malpas, J. C. N. Fletcher, J. R. Ali, and J. C. Aitchison (London: Geological Society of London Special Publication), 226, 73–100. doi:10.1144/GSL.SP.2004.226.01.05

Jiang, W., Yan, Q., Deng, L., Zhou, B., Xiang, Z., and Xia, W. (2019). Early Jurassic Mafic Intrusions in the Southern Youjiang Basin, SW China: Petrogenesis, Tectonic and Metallogenic Implications. *Minerals* 9 (12), 771. doi:10.3390/min9120771

Jochum, K. P., Nohl, U., Herwig, K., Lammel, E., Stoll, B., and Hofmann, A. W. (2005). GeoReM: A New Geochemical Database for Reference Materials and Isotopic Standards. *Geostand Geoanalyt Res.* 29 (3), 333–338. doi:10.1111/j.1751-908X.2005.tb00904.x

Karsli, O., Caran, Ş., Çoban, H., Şengün, F., Tekkanat, O., and Andersen, T. (2020). Melting of the Juvenile Lower Crust in a Far-Field Response to Roll-Back of the Southern Neotethyan Oceanic Lithosphere: the Oligocene Adakitic Dacites, NE Turkey. *Lithos* 370-371, 105614. doi:10.1016/j.lithos.2020.105614

Kudrass, H. R., Wiedicke, M., Cepek, P., Kreuzer, H., and Müller, P. (1986). Mesozoic and Cainozoic Rocks Dredged from the South China Sea (Reed Bank Area) and Sulu Sea and Their Significance for Plate-Tectonic Reconstructions. *Mar. Pet. Geology.* 3 (1), 19–30. doi:10.1016/0264-8172(86)90053-X

Lang, X., Deng, Y., Wang, X., Tang, J., Yin, Q., Xie, F., et al. (2020). Geochronology and Geochemistry of Volcanic Rocks of the Bima Formation, Southern Lhasa Subterrane, Tibet: Implications for Early Neo-Tethyan Subduction. *Gondwana Res.* 80, 335–349. doi:10.1016/j.gr.2019.11.005

Li, Q.-L., Li, X.-H., Wu, F.-Y., Yin, Q.-Z., Ye, H.-M., Liu, Y., et al. (2012a). In-situ SIMS U-Pb Dating of Phanerozoic Apatite with Low U and High Common Pb. *Gondwana Res.* 21 (4), 745–756. doi:10.1016/j.gr.2011.07.008

Li, Z.-X., Li, X.-H., Chung, S.-L., Lo, C.-H., Xu, X., and Li, W.-X. (2012b). Magmatic Switch-On and Switch-Off along the South China continental Margin since the Permian: Transition from an Andean-type to a Western Pacific-type Plate Boundary. *Tectonophysics* 532-535, 271–290. doi:10.1016/j.tecto.2012.02.011

Li, B., Zhao, K. D., Yang, S. Y., and Dai, B. Z. (2013). Petrogenesis of the Porphyritic Dacite from Ermiaogou Cu-Au deposit in Zijinshan Ore Field and its Metallogenetic Implications. *Acta Petrol. Sin.* 12 (29), 4167–4185. (in Chinese with English abstract).

Li, C.-F., Xu, X., Lin, J., Sun, Z., Zhu, J., Yao, Y., et al. (2014). Ages and Magnetic Structures of the South China Sea Constrained by Deep Tow Magnetic Surveys and IODP Expedition 349. *Geochem. Geophys. Geosyst.* 15 (12), 4958–4983. doi:10.1002/2014GC005567

Li, C.-F., Chu, Z.-Y., Guo, J.-H., Li, Y.-L., Yang, Y.-H., and Li, X.-H. (2015). A Rapid Single Column Separation Scheme for High-Precision Sr-Nd-Pb Isotopic Analysis in Geological Samples Using thermal Ionization Mass Spectrometry. *Anal. Methods* 7 (11), 4793–4802. doi:10.1039/C4AY02896A

Li, B., Jiang, S.-Y., Zhang, Q., Zhao, H.-X., and Zhao, K.-D. (2016). Geochemistry, Geochronology and Sr-Nd-Pb-Hf Isotopic Compositions of Middle to Late Jurassic Syenite-Granodiorites-Dacite in South China: Petrogenesis and Tectonic Implications. *Gondwana Res.* 35, 217–237. doi:10.1016/j.gr.2015.05.006

Li, F., Sun, Z., and Yang, H. (2018). Possible Spatial Distribution of the Mesozoic Volcanic Arc in the Present-Day South China Sea Continental Margin and its

Tectonic Implications. *J. Geophys. Res. Solid Earth* 123 (8), 6215–6235. doi:10.1029/2017jb014861

Ludwig, K. (2000). Users Manual for Isoplot/Ex: a Geochronological Toolkit for Microsoft Excel. *Berkeley Geochronol. Cent. Spec. Publ.* 1a, 53.

Ma, Q., Xu, Y.-G., Zheng, J.-P., Griffin, W. L., Hong, L.-B., and Ma, L. (2016). Coexisting Early Cretaceous High-Mg Andesites and Adakitic Rocks in the North China Craton: the Role of Water in Intraplate Magmatism and Cratonic Destruction. *J. Petrol.* 57 (7), 1279–1308. doi:10.1093/petrology/egw040

Miao, X.-Q., Huang, X.-L., Yan, W., Yang, F., Zhang, W.-F., Cai, Y.-X., et al. (2021). Late Triassic Dacites from Well NK-1 in the Nansha Block: Constraints on the Mesozoic Tectonic Evolution of the Southern South China Sea Margin. *Lithos* 398-399, 106337. doi:10.1016/j.lithos.2021.106337

Miles, A. J., Graham, C. M., Graham, C. M., Hawkesworth, C. J., Gillespie, M. R., and Hinton, R. W. (2013). Edinburgh Ion Microprobe, FEvidence for Distinct Stages of Magma History Recorded by the Compositions of Accessory Apatite and Zircon. *Contrib. Mineral. Petrol.* 166 (1), 1–19. doi:10.1007/s00410-013-0862-9

Miles, A. J., Graham, C. M., Hawkesworth, C. J., Gillespie, M. R., Hinton, R. W., and Bromiley, G. D. (2014). Apatite: A New Redox Proxy for Silicic Magmas? *Geochim. Cosmochim. Acta* 132, 101–119. doi:10.1016/j.gca.2014.01.040

O'Sullivan, G., Chew, D., Kenny, G., Henrichs, I., and Mulligan, D. (2020). The Trace Element Composition of Apatite and its Application to Detrital Provenance Studies. *Earth-Science Rev.* 201, 103044. doi:10.1016/j.earscirev.2019.103044

Pan, L.-C., Hu, R.-Z., Wang, X.-S., Bi, X.-W., Zhu, J.-J., and Li, C. (2016). Apatite Trace Element and Halogen Compositions as Petrogenetic-Metallogenic Indicators: Examples from Four Granite Plutons in the Sanjiang Region, SW China. *Lithos* 254-255, 118–130. doi:10.1016/j.lithos.2016.03.010

Peng, X., Li, C.-F., Shen, C., Li, K., Zhao, Z., and Xie, X. (2020). Anomalous Lower Crustal Structure and Origin of Magmatism in the southeastern Margin of the South China Sea. *Mar. Pet. Geology.* 122, 104711. doi:10.1016/j.marpetgeo.2020.104711

Perugini, D., and Poli, G. (2012). The Mixing of Magmas in Plutonic and Volcanic Environments: Analogies and Differences. *Lithos* 153, 261–277. doi:10.1016/j.lithos.2012.02.002

Prowatke, S., and Klemme, S. (2006). Trace Element Partitioning between Apatite and Silicate Melts. *Geochim. Cosmochim. Acta* 70 (17), 4513–4527. doi:10.1016/j.gca.2006.06.162

Safonova, I., Maruyama, S., and Litasov, K. (2015). Generation of Hydrous-Carbonated Plumes in the Mantle Transition Zone Linked to Tectonic Erosion and Subduction. *Tectonophysics* 662, 454–471. doi:10.1016/j.tecto.2015.08.005

Savva, D., Pubellier, M., Franke, D., Chamot-Rooke, N., Meresse, F., Steuer, S., et al. (2014). Different Expressions of Rifting on the South China Sea Margins. *Mar. Pet. Geol.* 58, 579–598. doi:10.1016/j.marpetgeo.2014.05.023

Schlüter, H. U., Hinz, K., and Block, M. (1996). Tectono-stratigraphic Terranes and Detachment Faulting of the South China Sea and Sulu Sea. *Mar. Geology.* 130 (1), 39–78. doi:10.1016/0025-3227(95)00137-9

Shao, W.-Y., Chung, S.-L., Chen, W.-S., Lee, H.-Y., and Xie, L.-W. (2015). Old continental Zircons from a Young Oceanic Arc, Eastern Taiwan: Implications for Luzon Subduction Initiation and Asian Accretionary Orogeny. *Geology* 43 (6), 479–482. doi:10.1130/G36499.1

Sibuet, J.-C., Yeh, Y.-C., and Lee, C.-S. (2016). Geodynamics of the south China Sea. *Tectonophysics* 692, 98–119. doi:10.1016/j.tecto.2016.02.022

Sun, S.-S., and McDonough, W. F. (1989). Chemical and Isotopic Systematics of Oceanic Basalts: Implications for Mantle Composition and Processes. *Geol. Soc. Lond. Spec. Publ.* 42 (1), 313–345. doi:10.1144/GSL.SP.1989.042.01.19

Sun, W., Chiouting, L., Lipeng, Z., Renqiang, L., and Congying, L. (2018). The Formation of the South China Sea Resulted From the Closure of the Neo-Tethys: A Perspective From Regional Geology. *Acta Petrol. Sin.* 34 (12), 3467–3478 (in Chinese with English abstract).

Tang, X., Chen, L., Hu, S., Yang, S., Zhang, G., Shen, H., et al. (2014). Tectono-thermal Evolution of the Reed Bank Basin, Southern South China Sea. *J. Asian Earth Sci.* 96, 344–352. doi:10.1016/j.jseaes.2014.09.030

Tapponnier, P., Peltzer, G., and Armijo, R. (1986). On the Mechanics of the Collision between India and Asia. *Geol. Soc. Lond. Spec. Publ.* 19 (1), 113–157. doi:10.1144/GSL.SP.1986.019.01.07

Taylor, B., and Hayes, D. E. (1980). The Tectonic Evolution of the South China Basin. *Geophys. Monogr. Ser.* 23, 89–104. doi:10.1029/GM023p0089

Taylor, B., and Hayes, D. E. (1983). Origin and History of the South China Sea Basin. *Am. Geophys. Union* 27, 23–56. doi:10.1029/GM027p0023

Vervoort, J. D., Plank, T., and Prytulak, J. (2011). The Hf-Nd Isotopic Composition of marine Sediments. *Geochim. Cosmochim. Acta* 75 (20), 5903–5926. doi:10.1016/j.gca.2011.07.046

Wang, Y., Fan, W., Cawood, P. A., and Li, S. (2008). Sr-Nd-Pb Isotopic Constraints on Multiple Mantle Domains for Mesozoic Mafic Rocks beneath the South China Block Hinterland. *Lithos* 106 (3), 297–308. doi:10.1016/j.lithos.2008.07.019

Wei, X., Ruan, A., Zhao, M., Qiu, X., Wu, Z., and Niu, X. (2015). Shear Wave Velocity Structure of Reed Bank, Southern continental Margin of the South China Sea. *Tectonophysics* 644-645, 151–160. doi:10.1016/j.tecto.2015.01.006

Wei, W., Liu, C.-Z., Hou, Y.-F., Deng, C.-L., Yan, W., Li, X.-H., et al. (2021). Discovery of a Hidden Triassic Arc in the Southern South China Sea: Evidence for the Breakaway of a Ribbon Continent With Implications for the Evolution of the Western Pacific Margin. *Terra Nova*, 1–8. doi:10.1111/ter.12556

Winchester, J. A., and Floyd, P. A. (1976). Geochemical Magma Type Discrimination: Application to Altered and Metamorphosed Basic Igneous Rocks. *Earth Planet. Sci. Lett.* 28 (3), 459–469. doi:10.1016/0012-821X(76)90207-7

Wu, Z.-C., Gao, J.-Y., Li, J.-B., Zhang, T., Shen, Z.-Y., and Yang, C.-G. (2011). Characteristics of Magnetic Anomalies in the Northern South China Sea and Their Implications for Pre-cenozoic Tectonics. *Chin. J. Geophys.* 54 (6), 1112–1123. doi:10.1002/cjg2.1688

Xie, X., Xu, X., Zou, H., Jiang, S., Ming, Z., and Qiu, J. (2006). Early J2 Basalts in SE China: Incipience of Large-Scale Late Mesozoic Magmatism. *Sci. China Ser. D* 49 (8), 796–815. doi:10.1007/s11430-006-0796-4

Xu, X., O'Reilly, S. Y., Griffin, W. L., Wang, X., Pearson, N. J., and He, Z. (2007). The Crust of Cathaysia: Age, Assembly and Reworking of Two Terranes. *Precambrian Res.* 158 (1), 51–78. doi:10.1016/j.precamres.2007.04.010

Xu, Y., Wei, J., Qiu, H., Zhang, H., and Huang, X. (2012). Opening and Evolution of the South China Sea Constrained by Studies on Volcanic Rocks: Preliminary Results and a Research Design. *Chin. Sci. Bull.* 57 (24), 3150–3164. doi:10.1007/s11434-011-4921-1

Xu, C., Zhang, L., Shi, H., Brix, M. R., Huhma, H., Chen, L., et al. (2017). Tracing an Early Jurassic Magmatic Arc from South to East China Seas. *Tectonics* 36 (3), 466–492. doi:10.1002/2016TC004446

Yamamoto, S., Senshu, H., Rino, S., Omori, S., and Maruyama, S. (2009). Granite Subduction: Arc Subduction, Tectonic Erosion and Sediment Subduction. *Gondwana Res.* 15 (3), 443–453. doi:10.1016/j.gr.2008.12.009

Yamamoto, T. (2007). A Rhyolite to Dacite Sequence of Volcanism Directly from the Heated Lower Crust: Late Pleistocene to Holocene Numazawa Volcano, NE Japan. *J. Volcanology Geothermal Res.* 167 (1), 119–133. doi:10.1016/j.jvolgeores.2007.05.011

Yan, Q., Shi, X., Liu, J., Wang, K., and Bu, W. (2010). Petrology and Geochemistry of Mesozoic Granitic Rocks from the Nansha Micro-block, the South China Sea: Constraints on the Basement Nature. *J. Asian Earth Sci.* 37 (2), 130–139. doi:10.1016/j.jseaes.2009.08.001

Yan, Q., Shi, X., and Li, N. (2011). Oxygen and lead Isotope Characteristics of Granitic Rocks from the Nansha Block (South China Sea): Implications for Their Petrogenesis and Tectonic Affinity. *Isl. Arc* 20, 150–159. doi:10.1111/j.1440-1738.2010.00754.x

Yan, Q., Shi, X., and Castillo, P. R. (2014). The Late Mesozoic-Cenozoic Tectonic Evolution of the South China Sea: A Petrologic Perspective. *J. Asian Earth Sci.* 85 (2), 178–201. doi:10.1016/j.jseaes.2014.02.005

Yang, Y., Sun, J., Xie, L., Fan, H., and Wu, F. (2008). *In Situ* Nd Isotopic Measurement of Natural Geological Materials by LA-MC-ICPMS. *Sci. Bull.* 53 (7), 1062–1070. doi:10.1007/s11434-008-0166-z

Yang, Y.-h., Zhang, H.-F., Chu, Z.-Y., Xie, L.-w., and Wu, F.-Y. (2010). Combined Chemical Separation of Lu, Hf, Rb, Sr, Sm and Nd from a Single Rock Digest and Precise and Accurate Isotope Determinations of Lu-Hf, Rb-Sr and Sm-Nd Isotope Systems Using Multi-Collector ICP-MS and TIMS. *Int. J. Mass Spectrom.* 290, 120–126. doi:10.1016/j.ijms.2009.12.011

Yang, J.-H., Sun, J.-F., Zhang, J.-H., and Wilde, S. A. (2012). Petrogenesis of Late Triassic Intrusive Rocks in the Northern Liaodong Peninsula Related to Decratonization of the North China Craton: Zircon U-Pb Age and Hf-O Isotope Evidence. *Lithos* 153 (8), 108–128. doi:10.1016/j.lithos.2012.06.023

Yang, Y.-H., Wu, F.-Y, Wilde, S. A., Liu, X.-M., Zhang, Y.-B., Xie, L.-W., et al. (2009). *In situ* Perovskite Sr–Nd Isotopic Constraints on the Petrogenesis of the Ordovician Mengyin Kimberlites in the North China Craton. *Chem. Geol.* 264 (1), 24–42. doi:10.1016/j.chemgeo.2009.02.011

Yang, Y.-H., Wu, F.-Y., Yang, J.-H., Chew, D. M., Xie, L.-W., Chu, Z.-Y., et al. (2014). Sr and Nd Isotopic Compositions of Apatite Reference Materials Used in U-Th-Pb Geochronology. *Chem. Geology.* 385, 35–55. doi:10.1016/j.chemgeo.2014.07.012

Yang, F., Santosh, M., Glorie, S., Xue, F., Zhang, S., and Zhang, X. (2020). Apatite Geochronology and Chemistry of Luanchuan Granitoids in the East Qinling Orogen, China: Implications for Petrogenesis, Metallogenesis and Exploration. *Lithos* 378-379, 105797. doi:10.1016/j.lithos.2020.105797

Yao, B. C., Wan, L., and Wu, N. (2004). Cenozoic Plate Tectonic Activities in the Great South China Sea Area. *Geology. China* 31, 113–122. doi:10.1016/B978-0-08-028692-1.50009-3

Ye, Q., Mei, L., Shi, H., Camanni, G., Shu, Y., Wu, J., et al. (2018). The Late Cretaceous Tectonic Evolution of the South China Sea Area: An Overview, and New Perspectives from 3D Seismic Reflection Data. *Earth-Sci. Rev.* 187, 186–204. doi:10.1016/j.earscirev.2018.09.013

Yu, M., Yan, Y., Huang, C.-Y., Zhang, X., Tian, Z., Chen, W.-H., et al. (2018). Opening of the South China Sea and Upwelling of the Hainan Plume. *Geophys. Res. Lett.* 45 (6), 2600–2609. doi:10.1002/2017GL076872

Yu, Z.-Q., Chen, W.-F., Chen, P.-R., Wang, K.-X., Fang, Q.-C., Tang, X.-S., et al. (2019). Chemical Composition and Sr Isotopes of Apatite in the Xiangshan A-type Volcanic-Intrusive Complex, Southeast China: New Insight into Petrogenesis. *J. Asian Earth Sci.* 172, 66–82. doi:10.1016/j.jseaes.2018.08.019

Zafar, T., Rehman, H. U., Mahar, M. A., Alam, M., Oyebamiji, A., Rehman, S. U., et al. (2020). A Critical Review on Petrogenetic, Metallogenic and Geodynamic Implications of Granitic Rocks Exposed in north and east China: New Insights from Apatite Geochemistry. *J. Geodyn.* 136, 101723. doi:10.1016/j.jog.2020.101723

Zhang, G.-L., Luo, Q., Zhao, J., Jackson, M. G., Guo, L.-S., and Zhong, L.-F. (2018a). Geochemical Nature of Sub-ridge Mantle and Opening Dynamics of the South China Sea. *Earth Planet. Sci. Lett.* 489, 145–155. doi:10.1016/j.epsl.2018.02.040

Zhang, L., Wang, Y., Qian, X., Zhang, Y., He, H., and Zhang, A. (2018b). Petrogenesis of Mesoproterozoic Mafic Rocks in Hainan (South China) and its Implication on the Southwest Hainan-Laurentia-Australia Connection. *Precambrian Res.* 313, 119–133. doi:10.1016/j.precamres.2018.05.002

Zhang, X., Guo, F., Zhang, B., Zhao, L., Wu, Y., Wang, G., et al. (2020). Magmatic Evolution and post-crystallization Hydrothermal Activity in the Early Cretaceous Pingtan Intrusive Complex, SE China: Records from Apatite Geochemistry. *Contrib. Mineral. Petrol.* 175 (4), 35. doi:10.1007/s00410-020-1675-2

Zhang, X., Guo, F., Zhang, B., Zhao, L., and Wang, G. (2021). Mixing of Cogenetic Magmas in the Cretaceous Zhangzhou Calc-Alkaline Granite from Southeast China Recorded by *In-Situ* Apatite Geochemistry. *Am. Mineral.* 106 (10), 1679–1689. doi:10.2138/am-2021-7786

Zhao, M., Qiu, X., Xia, S., Xu, H., Wang, P., Wang, T. K., et al. (2010). Seismic Structure in the Northeastern South China Sea: S-Wave Velocity and Vp/Vs Ratios Derived from Three-Component OBS Data. *Tectonophysics* 480 (1), 183–197. doi:10.1016/j.tecto.2009.10.004

Zhou, D., Wang, W., Wang, J., Pang, X., Cai, D., and Sun, Z. (2006). Mesozoic Subduction-Accretion Zone in Northeastern south china Sea Inferred from Geophysical Interpretations. *Sci. China Ser. D* 49 (5), 471–482. doi:10.1007/s11430-006-0471-9

Zhou, Y., Liang, X., Kröner, A., Cai, Y., Shao, T., Wen, S., et al. (2015). Late Cretaceous Lithospheric Extension in SE China: Constraints from Volcanic Rocks in Hainan Island. *Lithos* 232, 100–110. doi:10.1016/j.lithos.2015.06.028

Conflict of Interest: The authors declare that the research was conducted in the absence of any commercial or financial relationships that could be construed as a potential conflict of interest.

Publisher's Note: All claims expressed in this article are solely those of the authors and do not necessarily represent those of their affiliated organizations, or those of the publisher, the editors and the reviewers. Any product that may be evaluated in this article, or claim that may be made by its manufacturer, is not guaranteed or endorsed by the publisher.